# FINAL REPORT
## ON
## NASA AMES GRANT NO. NCC2 - 795

PERIOD COVERING JANUARY 1993 THROUGH JUNE 1995

## AN INTEGRATED OPTIMUM DESIGN APPROACH FOR HIGH SPEED PROP ROTORS

BY

ADITI CHATTOPADHYAY, ASSOCIATE PROFESSOR

AND

THOMAS R. MCCARTHY, GRADUATE RESEARCH ASSOCIATE

DEPARTMENT OF MECHANICAL AND AEROSPACE ENGINEERING

ARIZONA STATE UNIVERSITY

TEMPE, ARIZONA   85287 - 6106

AUGUST 1995

SEP 1 2 1995

# TABLE OF CONTENTS

# LIST OF TABLES

# LIST OF FIGURES

# 1. Introduction

There are many design requirements associated with tilt-rotor performance including a low disc loading in the hover configuration and the ability to rotate the rotors forward to achieve cruise speeds up to 450 knots [1]. The problem becomes more complex since in vertical flight and in hover, a large portion of the rotor is directly over the wing which produces a large downwash effect upon the wing. The downwash effect increases thrust requirement of the aircraft by approximately 10 - 12 percent [2]. Other problems associated with this configuration are related to high helical tip Mach numbers ($M_{tip}$) which represent a critical performance issue in high speed cruise (350 - 450 knots). Aeroelastic stability is another important consideration in the design of tilt-rotors. Due to the large thrust requirement in hover, the prop-rotors have a much greater radius than standard propellers. This increases the tip speed which in cruise may cause individual blade flutter or a coupled flexible motion between the rotor, wing and pylon known as whirl flutter. Also, blade sweep which is introduced for improvements in aerodynamic performance can be detrimental for aeroelastic stability. Since civil tiltrotors are required to be stable at a 20 percent margin above their dive speed, this means that the flutter speed must be in the order of 620 knots for a tiltrotor with a cruise speed of 450 knots.

There are several different techniques which can be used to address these issues. For example, the tip Mach number can be reduced through rotor tip speed reduction or through the use of blade sweep which reduces the effective Mach number. Another alternative is to increase the drag divergence Mach number ($M_{dd}$) at the tip to value above $M_{tip}$. This can be accomplished through reductions in the blade thickness. However, each of these options will adversely affect the hover performance, drive system weight or aeroelastic stability of the rotor blade. In the helicopter mode, to maintain a high figure of merit in hover, the solidity of the blade must be increased since thinner airfoils are used for maintaining efficiency in cruise. Due to such conflicting requirements between hover, conversion and airplane mode prop-rotor performance, the use of formal numerical optimization techniques is appropriate for studying the design trade-offs associated with the development of high speed tilt-rotors.
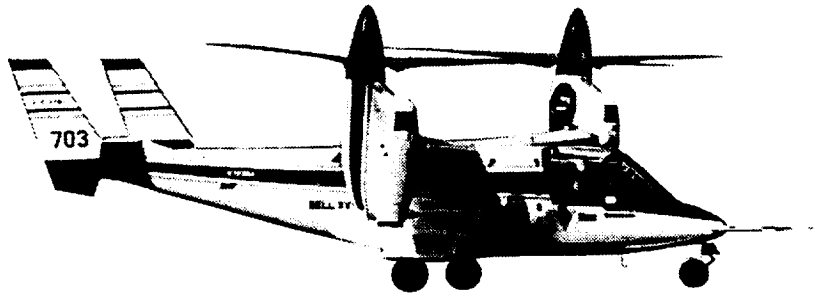
Figure 1 XV-15 tiltrotor in helicopter mode
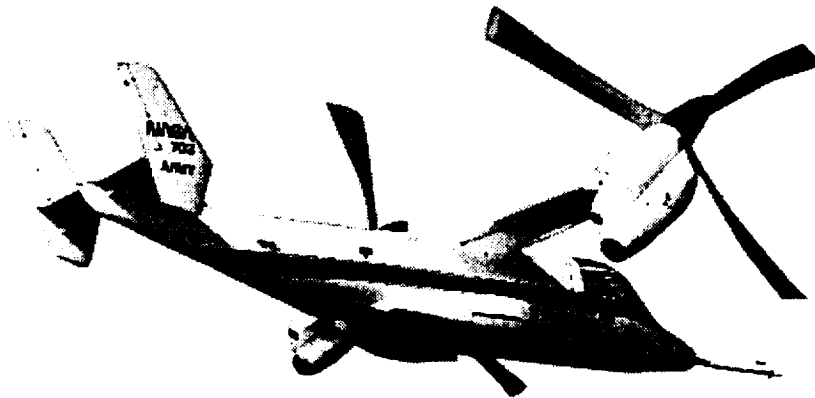


Figure 2 XV-15 tiltrotor in transition/conversion mode
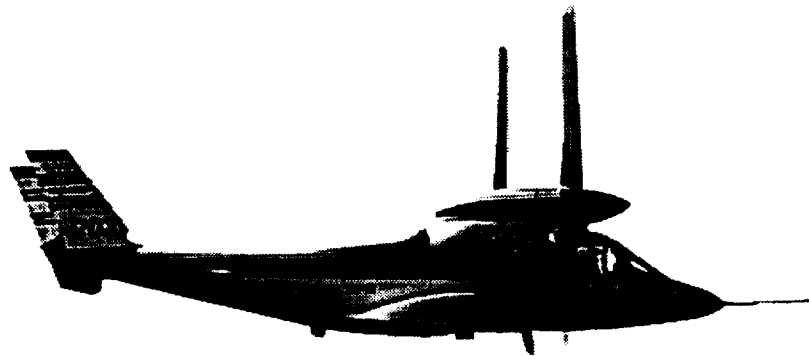


Figure 3 XV-15 in cruise mode

2

## 2. Objectives

The objective of this study is to develop an optimization procedure for high-speed and civil tilt-rotors by coupling all of the necessary disciplines within a closed-loop optimization procedure. Both simplified and comprehensive analysis codes are used for the aerodynamic analyses. The structural properties are calculated using in-house developed algorithms for both isotropic and composite box beam sections. The major objectives of this study are as follows:

1. Aerodynamic Optimization: Investigate the effects of blade aerodynamic characteristics on cruise and hover performance of prop-rotor aircraft using the classical blade element momentum approach with corrections for the high lift capability of rotors/propellers.

2. Coupled Aerodynamic/Structures Optimization: Develop a multilevel hybrid optimization technique for the design of prop-rotor aircraft. The design problem is decomposed into a level for improved aerodynamics with continuous design variables and a level with discrete variables to investigate composite tailoring. The aerodynamic analysis is based on that developed in the first objective and the structural analysis is performed using an in-house code which models a composite box beam. The results are compared to both a reference rotor and the optimum rotor found in the purely aerodynamic formulation (objective 1).

3. Multipoint Optimization: Extend the multilevel optimization procedure of objective 2 to a multipoint design problem. Include hover, cruise and take-off as the three flight conditions to be simultaneously maximized.

4. Coupled Rotor/Wing Optimization: Using the comprehensive rotary wing code, CAMRAD, develop an optimization procedure for the coupled rotor/wing performance in high speed tilt-rotor aircraft. The developed procedure contains design variables which define the rotor and wing planforms.

These objectives have all been achieved and the details of these investigations are presented in the next four sections.

3

# 3. Aerodynamic Optimization

The objective of this research effort is to explore the use of a simpler computational tool limited to aerodynamic performance only as one level of a multilevel based optimum design problem. Ultimately the results of this analysis, in a complete formulation, would represent an input to a more comprehensive structural and aeroelastic representation of the rotor characteristics. The results of this research effort represent evaluation of the suitability of optimization procedures to improve the aerodynamic performance of high speed prop-rotors by including all aerodynamic parameters as design variables. For example, blade chord, twist, thickness and camber distributions are allowed to vary during the design optimization procedure. Since the design involves multiple objective functions, a multiobjective function formulation technique is used. Necessary side constraints are imposed on the design variables, during optimization, to prevent unrealistic values. However, in a multidisciplinary coupled problem, based on multilevel decomposition formulation, more realistic constraints on chord, twist, thickness and camber would be obtained from the optimal sensitivity parameters or the coordination constraint equations linking this formulation to the structural and aeroelastic representations in the other optimization levels.

## 3.1 Optimization Problem

The objectives of this study are to maximize the propulsive efficiency in high speed cruise ($\eta_c$) and the figure of merit in hover (FM). Two different forward speeds are used to represent the high speed cruise flight condition corresponding to 300 knots and 400 knots. In case of the 300 knots forward speed condition, the optimization is first performed individually for both hover and cruise. Then a formal multiobjective function formulation technique is used to simultaneously maximize the hover figure of merit and cruise propulsive efficiency. The multiobjective formulation technique is also used in case of the 400 knots forward speed. Constraints are imposed on the rotor thrust in both hover and in high speed cruise. The blade is discretized and the values of chord (c), twist ($\theta$), thickness to chord ratio (t/c) and zero lift angle of attack ($\alpha_{zl}$) at each segment are used as design variables. The optimization problem is summarized as follows.

Maximize        $FM(\Phi), \eta_c(\Phi)$

subject to      $T_h = (T_h)_{ref}$

                $T_c = (T_c)_{ref}$

where $\Phi = [c(y), \theta(y), \alpha_{zl}(y), t/c(y)]$ is the design variable vector and the subscript 'ref' is used to indicate reference or baseline rotor values.

### 3.2 Multiobjective Formulation

Since the optimization problem involves more than one design objective, the objective function formulation is more complicated. In most of the existing work, the individual objective functions are combined using weight factors in a linear fashion. Such methods are judgmental as the answer depends upon the weight factors which are often hard to justify. Therefore, the problem is formulated using the Kreisselmeier-Steinhauser (K-S) function approach [3]. Using this function the multiple objective functions and constraints are transformed into a single envelope function which is then minimized using unconstrained optimization techniques. The K-S function has been found to perform extremely well by the authors for multiobjective rotary wing optimization problems [4,5].

The first step in formulating the objective function in the Kreisselmeier-Steinhauser (K-S) function approach involves transformation of the original objective functions into reduced objective functions. When the individual objective functions are to be minimized, these reduced objective functions assume the following form.

$$F_k^*(\Phi) = \frac{F_k(\Phi)}{F_{k_o}} - 1.0 - g_{max} \leq 0 \qquad\qquad k = 1, \ldots, NF_{min} \qquad\qquad (1a)$$

When the individual objective functions are to be maximized, the reduced objective functions are as follows.

$$F_k^*(\Phi) = 1.0 - \frac{F_k(\Phi)}{F_{k_o}} - g_{max} \leq 0 \qquad\qquad k = 1, \ldots, NF_{max} \qquad\qquad (1b)$$

5

where $F_{k_0}$ represents the value of the original objective function $F_k$ calculated at the beginning of each iteration and $\Phi$ is the design variable vector. The quantity $g_{max}$ is the value of the largest constraint corresponding to the original constraint vector, $g_j(\Phi)$ (j = 1, 2, $\cdots$ , NC), and is held constant during each iteration. These reduced objective functions are analogous to constraints, therefore a new constraint vector $f_m(\Phi)$ (m = 1, 2, $\cdots$ , M where M = NC + NF) is introduced which includes the original constraints and the constraints introduced by the reduced objective functions (Eqns. 1). The design variable vector remains unchanged. The new objective function to be minimized is defined using the K-S function as follows.

$$F_{KS}(\Phi) = f_{max} + \frac{1}{\delta} \ln \sum_{m=1}^{M} \exp\left[\delta(f_m - f_{max})\right] \tag{2}$$

where $f_{max}$ is the largest constraint corresponding to the new constraint vector, $f_m(\Phi)$, and in general is not equal to $g_{max}$. The optimization procedure is as follows. Initially in an infeasible design space, where the original constraints are violated, the constraints due to the reduced objective functions (Eqns. 1) are satisfied, i.e. $g_{max}$ is negative. Once the original constraints are satisfied, the constraints due to the reduced objective functions become violated (positive). When this happens, the optimizer attempts to satisfy these constraints introduced by the reduced objective functions and in doing so, minimizes the original objective functions ($F_k$). The multiplier $\delta$ is analogous to a draw-down factor where $\delta$ controls the distance from the surface of the K-S objective function to the surface of the maximum constraint function. When $\delta$ is large, the K-S function closely follows the surface of the largest constraint function. When $\delta$ is small, the K-S function includes contributions from all violated constraints. Although in this traditional formulation, the objective functions and constraints are coupled in a less judgmental manner, it must be noted that weight factors can be introduced for the objective functions and/or constraints through Eqns. 1. For a given set of weighting factors, the K-S function only selects one point on a locus of optimum points on a plot of hover figure of merit versus propulsive efficiency. However, as in linear combinations of objective functions, weight factors can be used in the K-S

formulation to emphasize the importance of one or more objective functions over the remaining objective functions. In the present formulation, no such weight factors are used.

## 3.4 Analysis

The aerodynamic formulation is based on the two dimensional compressible aerodynamic representation developed by Smith [6] and later used by Talbot [7] in the formulation of an axial flow performance analysis. The modifications by Talbot include an empirical correction to two dimensional stall behavior in order to represent the high lift capability demonstrated by rotors and propellers. Compressibility and Reynold's number effects are included in this formulation. The blade element theory used in the algorithm is due to Glauert [8]. In this formulation, the sectional lift and drag are resolved into elemental thrust and torque for each section of the blade. The force and momentum equations for thrust and torque assume the following form.

$$dT_1 = 4\pi r \rho_\infty (V_\infty + \upsilon_i) \upsilon_i dr \tag{3}$$

$$dT_2 = \frac{1}{2} \rho_\infty W^2 c [c_l \cos(\alpha_l) - c_d \sin(\alpha_l)] dr \tag{4}$$

$$dQ_1 = 4\pi r^2 \rho_\infty (V_\infty + \upsilon_i) u_T dr \tag{5}$$

$$dQ_2 = \frac{1}{2} \rho_\infty W^2 c [c_l \sin(\alpha_l) + c_d \cos(\alpha_l)] r dr \tag{6}$$

where dT, dQ and dr represent the section thrust, torque and element length, respectively, W is the resultant velocity, $V_\infty$ is the forward velocity and $\upsilon_i$ and $u_T$ represent the inflow and swirl velocities, respectively. The chord length and radial locations are denoted c and r, respectively and $\rho_\infty$ is the density of air. The sectional coefficients of lift and drag are $c_l$ and $c_d$, respectively and $\alpha_l$ is the local inflow angle of the blade section. The subscripts (1) and (2) correspond to the momentum and force equations, respectively, for thrust and torque. Detailed expressions for the coefficients of lift and drag ($c_l$ and $c_d$), which represent the high lift capability of rotary wings in post stall angle of attack region, are found in Ref. 6. This system of equations is then used to solve for the inflow and swirl velocities by equating the thrust and torque as follows:

$$dT_1 = dT_2 \tag{7}$$

$$dQ_1 = dQ_2 \tag{8}$$

In the initial study performed by Smith [6] an empirical fit was performed on NACA 63 and 64 series airfoil families in order to supply a functional relationship between maximum lift coefficient and the sectional thickness and camber for incompressible flow. These functional relationships were later modified by Talbot [7] to model the Advanced Tiltrotor Blades (ATB) [9,10]. This representation is suitable only for conceptual design and it is recognized by the authors that a more sophisticated airfoil property representation is desirable during detailed design. However, as the baseline XV-15 rotor system utilizes airfoils of this general capability, it is felt that this representation is adequate to demonstrate the capability of an optimization procedure to generate a feasible design. The analysis is easily implemented within an optimization procedure and offers significant computational advantages compared to more comprehensive analysis procedures. The adequacy of this representation is demonstrated in Figs. 4 and 5, where this relatively simplistic formulation is shown to correlate very well with measured axial flow performance of the XV-15 rotor system in both hover and in airplane mode from tests conducted at the Outdoor Aerodynamic Research Facility (O.A.R.F.) and from wind tunnel test data obtained at NASA Ames Research Center [9,10]. This representation of the rotor, which is representative of the original design point of the XV-15 tiltrotor, is used as the baseline, or reference, rotor for both the 300 and 400 knots cases. Further, the results obtained using this approach are comparable with results obtained by Dadone et al. using comprehensive rotorcraft analyses [1]. Other elementary algorithms have been proposed to model the post stall delay due to rotation [11].

### 3.5 Optimization Implementation

A nonlinear programming procedure, based on the method of feasible directions, is used for the optimization [12]. During optimization, several evaluations of the objective function and constraints are necessary to obtain a feasible design. Therefore, the process can become computationally expensive if exact analyses are performed for every function evaluation. An approximate analysis technique is therefore implemented in the calculations of the objective functions and the constraints. The approximate analysis used in this study is based on a two point exponential procedure [13].

8
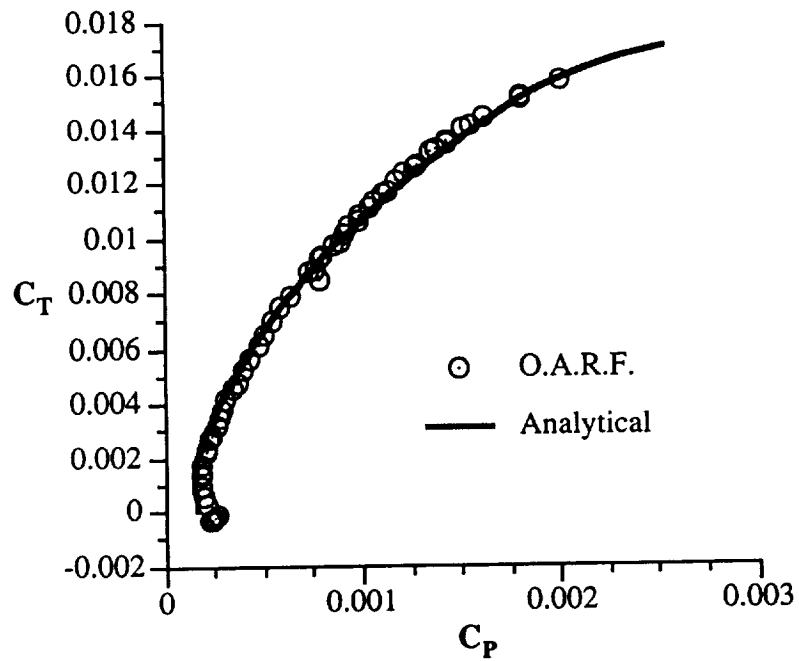
Figure 4  Comparison of analytical and experimental thrust in hover

**Sea Level Standard**
**J = 2.01**
**(μ = 0.640)**
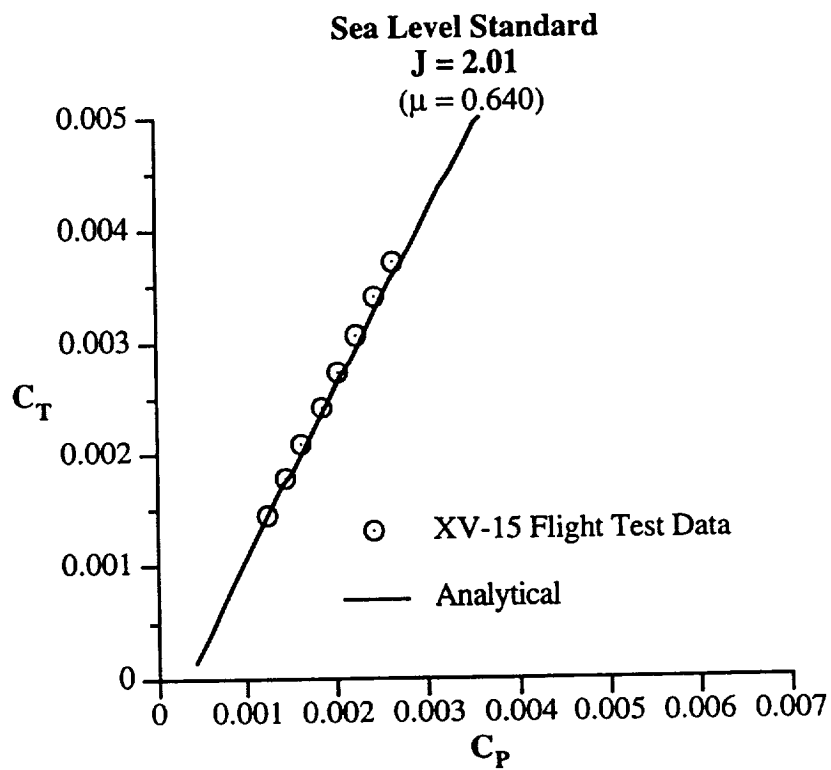


Figure 5  Cruise propulsive efficiency correlation

## 3.6 Results and Discussions

The reference rotor used is the original XV-15 prop-rotor [9,10]. In both airplane mode forward flight conditions the rotational speed is 421 RPM and the aircraft altitude is 25,000 feet. A vehicle weight of 13,000 lb. and aircraft lift to drag ratio (L/D) of 8.4 is assumed for both cruise flight conditions. Therefore, the thrust in cruise is constrained to be 774 lb. for the two engine aircraft. In hover, the aircraft is assumed to be operating at sea level conditions with a rotational speed of 570 RPM and a 12 percent down load effect from the rotor/wing interaction. The thrust in hover for the two rotor aircraft is therefore constrained to be 7280 lb. To ascertain the credibility of the optimization procedure as a design tool, the first problems addressed are the optimization of the XV-15 prop-rotor, initially for hover only and for 300 knots cruise operation, next. The intent of these single objective function optimization procedures is to demonstrate the capability of the optimization procedure in identifying the planform characteristics known to be optimum for both a helicopter in hover and a propeller. The multiobjective function formulation optimization procedure is then performed first for the 300 knots cruise condition and then for the 400 knots forward flight condition. These flight conditions are summarized in Table 1. The blade is discretized into 10 segments. The discrete nodal values of chord (c), twist, relative to the twist at the $\bar{y} = 0.75$ radial location, ($\theta$), thickness to chord ratio (t/c) and zero lift angle of attack ($\alpha_{zl}$) are used as design variables yielding a total of 44 design variables. The following side constraints are imposed on the design variables throughout the blade span.

$$0.001 \leq c/R \leq 0.50 \tag{9a}$$

$$-15° \leq \theta \leq 45.0° \tag{9b}$$

$$0.05 \leq t/c \leq 0.40 \tag{9c}$$

$$-5.0° \leq \alpha_{zl} \leq 3.0° \tag{9d}$$

It must be noted that the lower bound of c/R = 0.001 listed above (9a) is included to consider the aerodynamic only optimization case. Although the same values are used as side constraints for the chord in the other optimization cases as well so that meaningful comparisons of the chord distributions can be made, the actual chord values in these cases never approach this bound.

10

Table 1 Summary of Flight Conditions (Objective 1)

| Vehicle Weight | 13,000 lb |
|---|---|
| Blade Radius | 12.5 ft |
| | |
| Hover Altitude | Sea level |
| Hover Thrust, $T_h$ | 7280 lb |
| Hover Rotational Speed | 570 RPM |
| | |
| Cruise Altitude | 25,000 ft |
| Cruise Thrust, $T_c$ | 774 lb |
| Cruise Rotational Speed | 421 RPM |

The optimization results for the following cases: hover, airplane mode with forward speed of 300 knots and multiobjective formulation (hover and cruise), also at 300 knots, are presented in Figs. 6-10. Figure 6 shows that the single objective function formulation produces designs with significant performance improvements. In case of hover, the figure of merit is increased by 9.2 percent and in case of airplane mode the propulsive efficiency is increased by 8.7 percent. In the multiobjective function case, as expected, the improvements are significant, but not as dramatic as in the single objective function cases. In this case, the figure of merit is increased by 7.7 percent and the propulsive efficiency is increased by 3.7 percent. It is important to note that the multiobjective formulation is capable of retaining the bulk of the hover performance improvement, but the propulsive efficiency is apparently limited by the solidity requirements for hover.

Examinations of the basic planform generated by this procedure in Fig. 7 shows that the optimization procedure is capable of identifying the classic optimal planform for both hover and cruise operations. In the case of hover, the planform varies as the inverse of the radial location and in the cruise case (propeller mode), the root chord is driven almost to zero. As shown in the figure, the multiobjective function planform is more closely related to the hover planform although the airplane mode efficiency objective function does reduce the chord values from root to midspan. The reason the multiobjective planform more closely models the hover only solution is due to the fact that a much larger solidity is necessary to achieve the required thrust in hover. The outboard chord reduction, relative to the reference, in the multiobjective design is a reflection of the lack of a maneuver margin requirement in the optimization problem formulation. Figure 7 not only shows

11

the optimizer's ability to recognize the classical solution, but also the root chord values in the case of the cruise only optimization demonstrate the necessity of imposing realistic constraints on the design variables during the optimization process. It is obvious more practical side constraints are necessary for a realistic design.
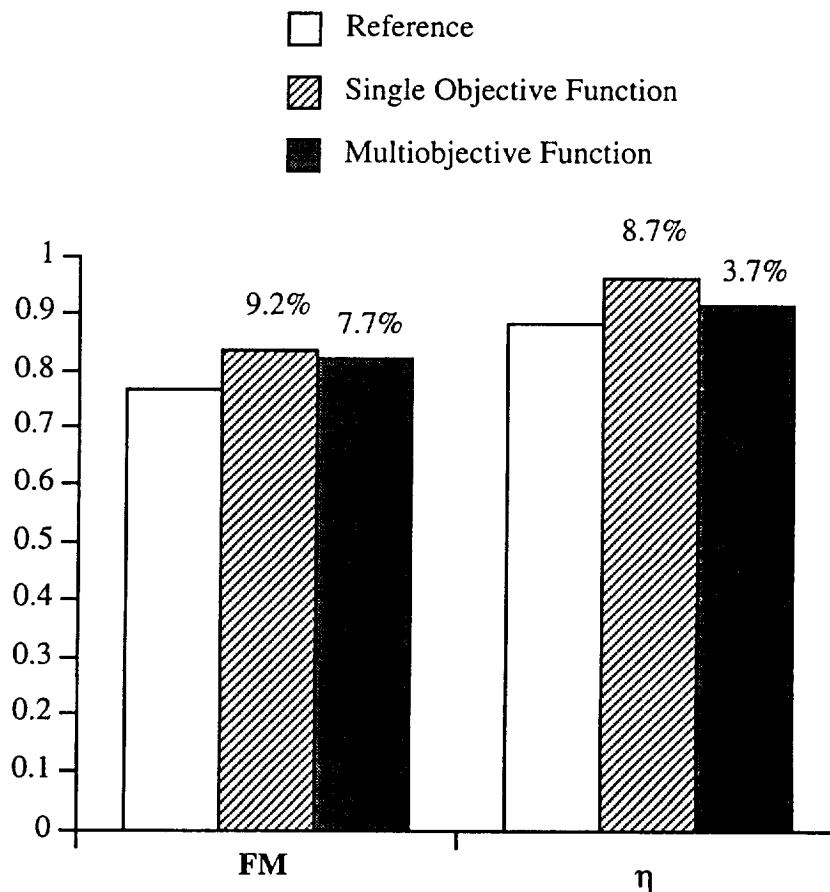


Figure 6  Summary of optimum results

The twist ($\theta$) distributions for the reference and the three optimum rotors are presented in Fig. 8. In case of the hover only optimization, the classical solution, which varies as the inverse of the radial location, is once again achieved. In the airplane mode, the twist distribution is much more linear which is expected due to the high inflow velocity at the forward flight condition. The distribution in the multiobjective formulation case shows the trade-offs associated with these two conflicting requirements. From root to mid span, the distribution is much closer to the airplane mode twist, however, at outboard locations the optimal twist is nearly identical to the hover only

12

case. The reason the multiobjective optimal twist distribution more closely follows the cruise only case is due to the fact that the rotor planform is sized for hover and therefore in order to simultaneously achieve high propulsive efficiency it is necessary to twist the blade according to the requirements in cruise. It is noteworthy that the optimal twist distribution in case of the multiobjective formulation is almost identical to the reference rotor.
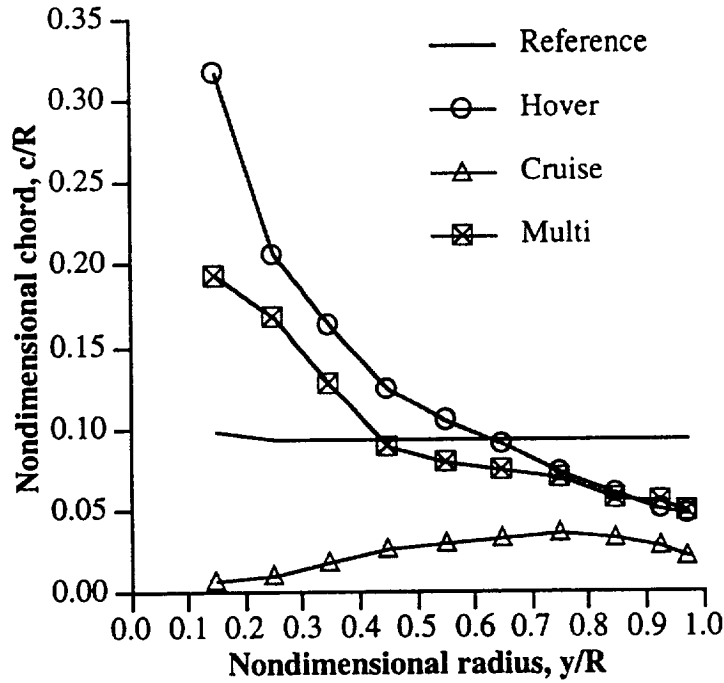


Figure 7  Chord distributions

Figure 9 shows that the zero lift angle of ($\alpha_{zl}$) attack is drastically reduced (made more negative) throughout the blade span. This effectively increases the camber of the airfoil which improves the lift-to-drag ratio and improves performance. In cruise, there is an increase in $\alpha_{zl}$ from the reference value at the blade tip. The reason for the resulting decrease in camber at the tip can be explained as the optimizer's effort in avoiding a reduction of the drag divergence Mach number ($M_{dd}$) to values below operational Mach number at this location. Once again, the multiobjective formulation more closely follows the hover distribution except at radial locations which require high Mach drag divergence number (e.g. near the tip). The results clearly demonstrate the trade-offs associated between the two flight conditions. It must be noted that the

13

zero lift angle of attack distributions presented in this paper are achieved primarily through blade camber and a more comprehensive study would have to include considerations of not only maximum camber requirements but must also include constraints on the moment coefficients as well.
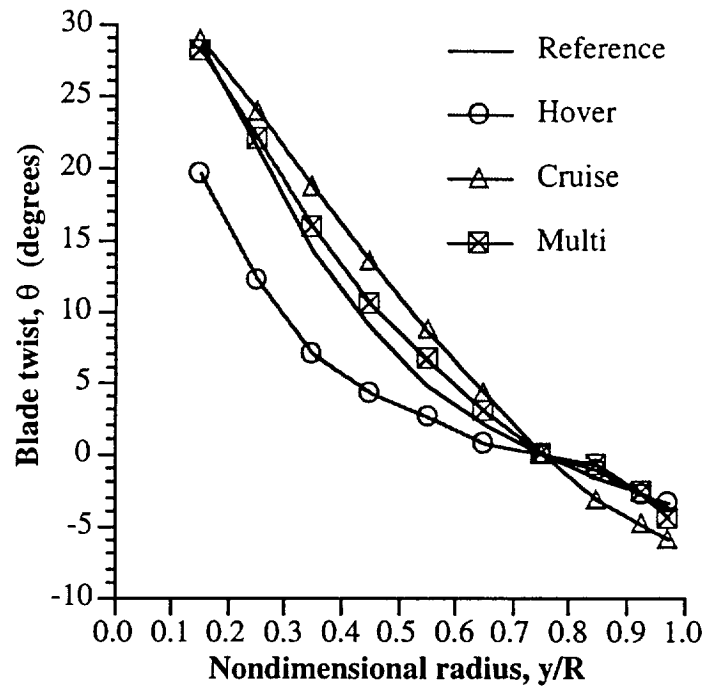


Figure 8 Twist distributions

Figure 10 shows the thickness to chord distributions (t/c) where it is seen that the blade thickness is significantly decreased in all cases, except at the blade tip. These decreases are an attempt to improve the rotor performance by decreasing the profile drag through reductions in the airfoil thickness. It is of interest to note that the multiobjective case is heavily biased towards the hover solution. This is explained as follows, since no weight factors are used in the K-S objective function formulation and all of the objective functions and constraints are normalized to unitary values, the optimization procedure is driven primarily by the dominance of the hover thrust requirement.
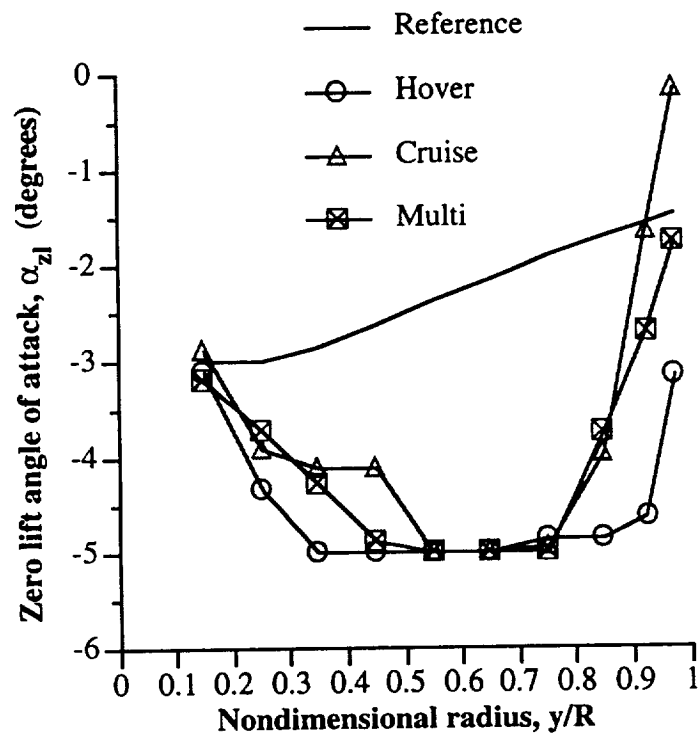
Figure 9  Zero lift angle of attack distributions
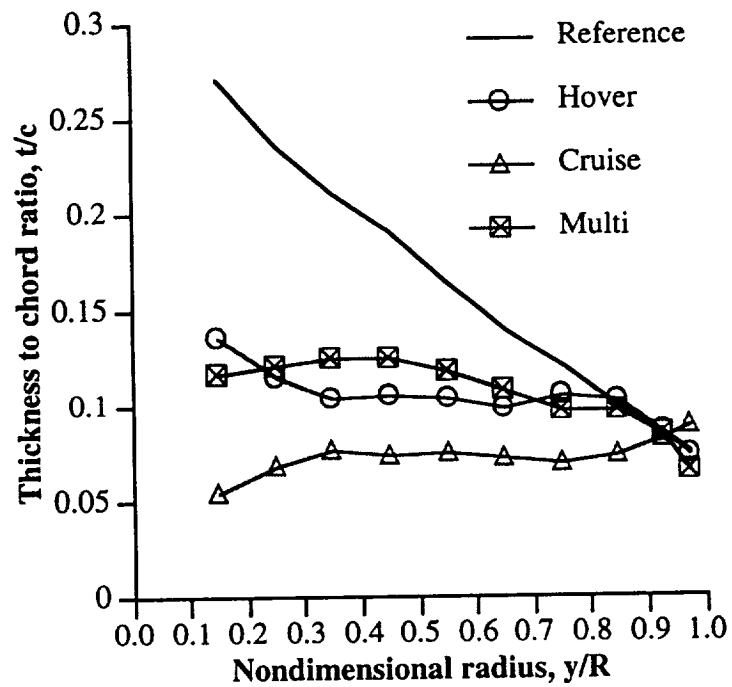


Figure 10  Thickness to chord ratio distributions

The final optimization case is performed for the simultaneous maximization of the hover figure of merit and propulsive efficiency of the XV-15 rotor at a forward speed of 400 knots. Results are compared with a reference rotor with the same planform as used in the 300 knots case and also the optimum rotor obtained from the multiobjective function formulation case at 300 knots. In Fig. 11 it is shown that the increase of 5.5 percent in the hover figure of merit, in case of the 400 knots cruise condition, is not as large as in case of the 300 knots cruise condition (7.7 percent). It is further shown that although the blade was originally designed for 300 knots, the same level of efficiency can be achieved at 400 knots after optimization (0.5 percent increase). The reason this increase in the figure of merit, from reference to optimum, is not as large in the case of the 400 knots cruise condition is due to the more stringent requirements of the cruise condition.
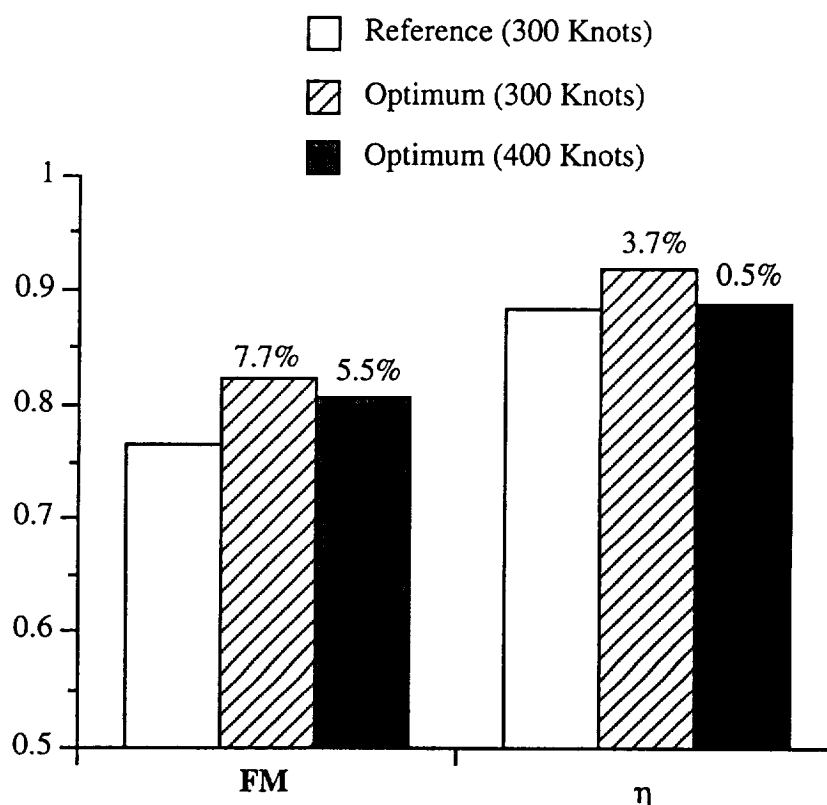


Figure 11 Comparison of optimum results

The chord distributions for the reference and the optimum rotors for the cruise speed of 400 knots are presented in Fig. 12. The multiobjective case with a cruise speed of 300 knots is

16

presented for comparison. The figure shows significant changes in chord from 300 to 400 knots designs. In case of the 400 knots forward flight condition, the chord is increased from midspan to outboard. The drastic reduction in chord at the root is due to an inability of the optimizer to find a satisfactory, that is, unstalled solution consistent with the cruise requirements.

The effective chordwise angle of attack ($\alpha$) distribution in hover is shown in Fig. 13 where

$$\alpha(\bar{y}) = \theta(\bar{y}) + \theta_{75} - \alpha_1(\bar{y}) - \alpha_{zl}(\bar{y}) \tag{10}$$

and $\theta_{75}$ is the collective pitch. From the figure it is seen that the effective angle of attack at the root in case of the reference blade and the 400 knot multiobjective optimization case is much higher than the effective angle of attack of either the hover only optimization case or the 300 knot multi-objective optimization case.
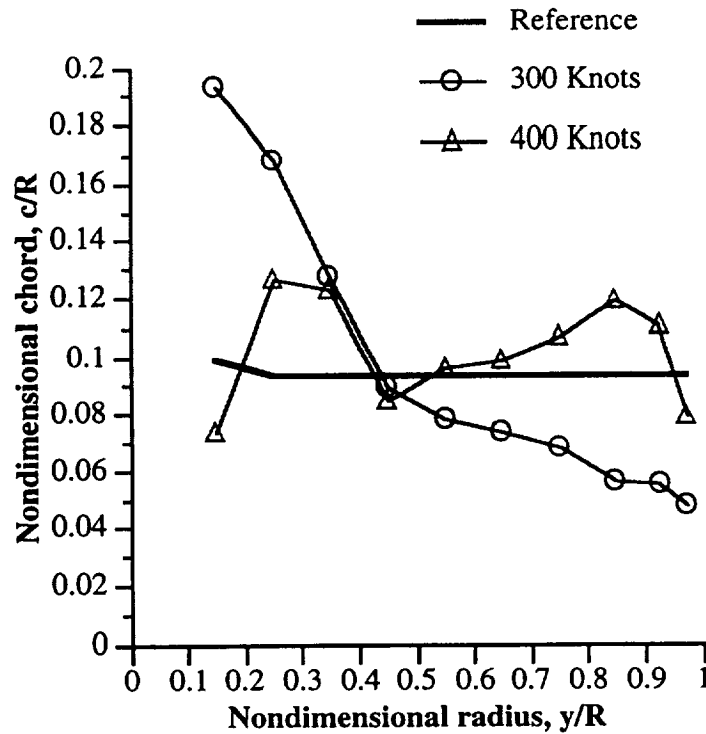


Figure 12  Chord distributions

The sectional lift-to-drag coefficient ratio ($c_l/c_d$) is presented in Fig. 14 and indicates that this large angle of attack at the root causes blade stall. The optimizer attempts to overcome this problem by reducing the root chord in an effort to decrease the stall drag penalty. The decreased values of

17

the chord, from reference to optimum, in the 400 knot multiobjective case can be explained by examining Figs. 15 and 16. It is seen in Fig. 15 that in case of the reference blade at 400 knots, the effective chordwise angle of attack ($\alpha$) in cruise is very small over the midspan of the blade and therefore this portion of the blade provides very little lift (Fig. 16). By reducing the chord in the optimum blade over the midspan region, the angle of attack is redistributed more uniformly throughout the blade. As a result the lift is more evenly distributed and the performance is improved.
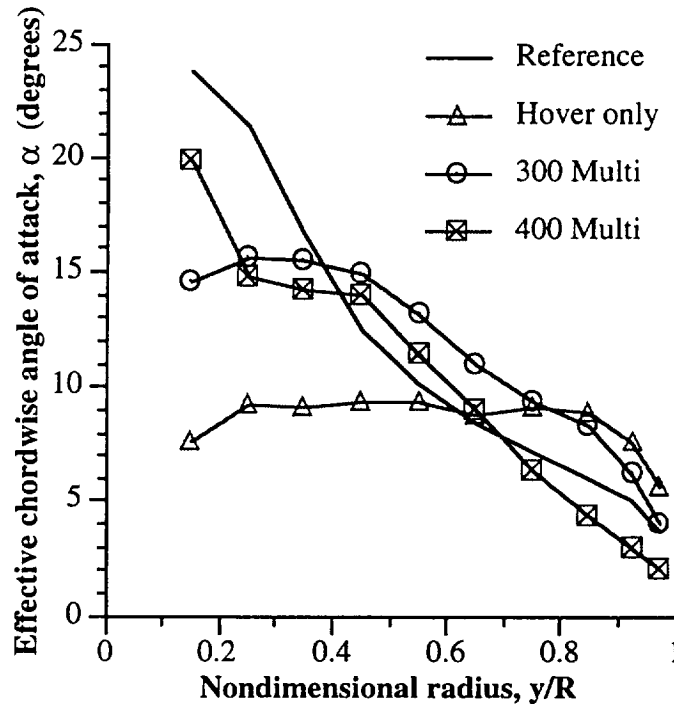


Figure 13  Effective chordwise angle of attack in hover

The twist distributions are shown in Fig. 17. From the figure it is seen that the optimum twist distribution for the 400 knots case has slightly less total twist than the reference rotor. The distribution is also more linear, compared to the reference. This reduced twist and linearity result from the higher axial advance ratio. To generate more thrust from the midspan sections, the angle of attack is increased slightly in this region. This has the effect of making the overall twist distributions more linear. Again, the similarities in the distributions between the reference and the 300 knots optimum rotor must be noted.
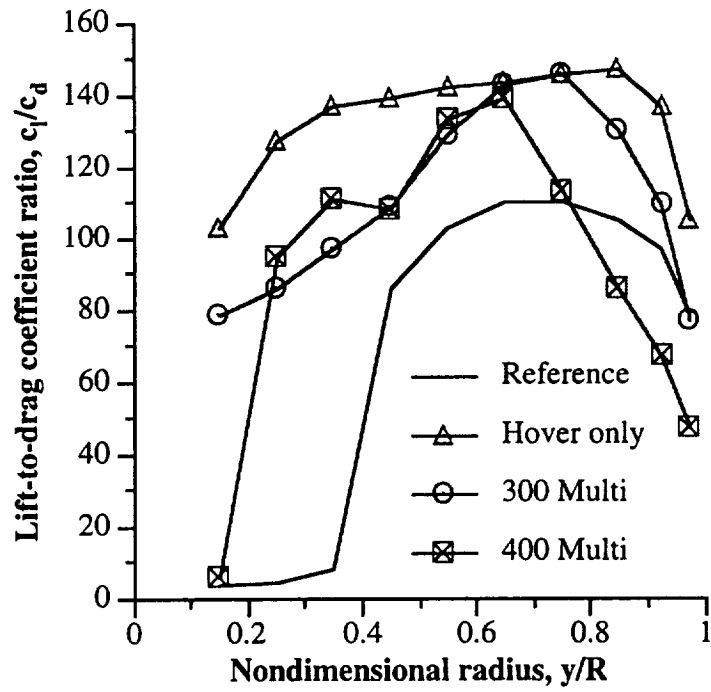
Figure 14  Sectional lift-to-drag coefficient distribution in hover
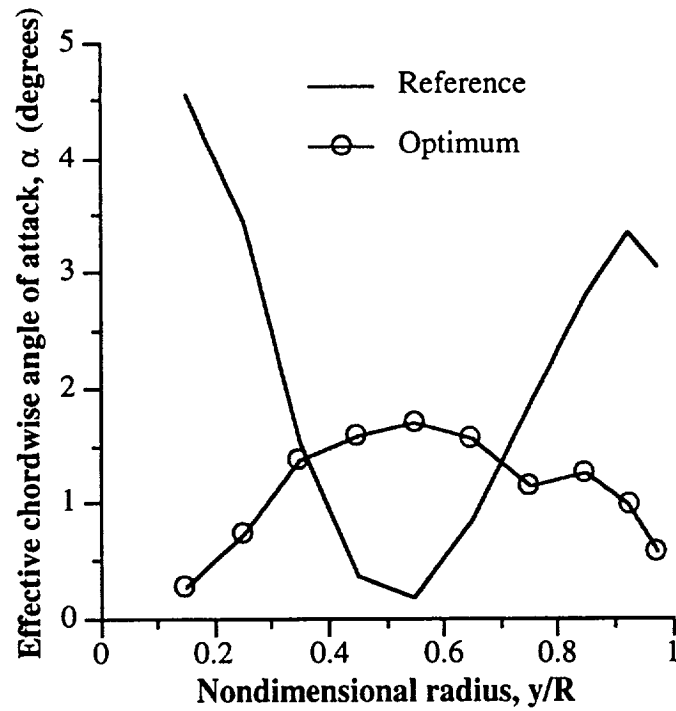


Figure 15  Effective chordwise angle of attack in cruise (400 knots)
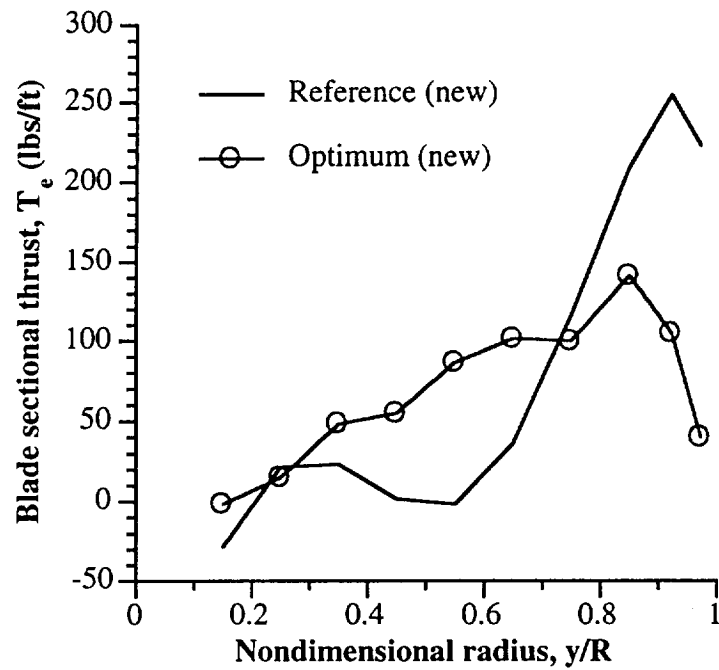
Figure 16  Blade thrust distribution in cruise (400 knots)
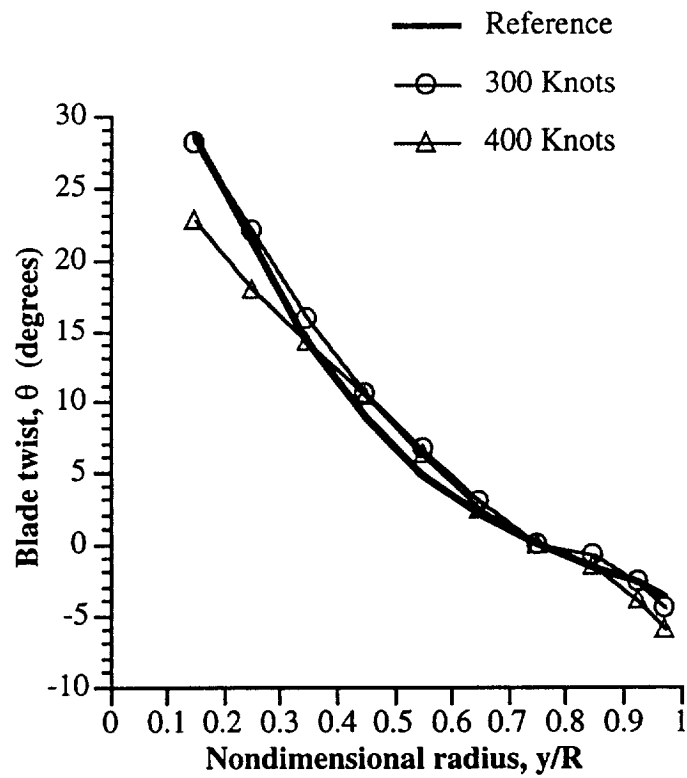


Figure 17  Twist distributions

20

Figure 18 shows the zero lift angle of attack ($\alpha_{zl}$) distributions. It is seen that the optimizer dramatically reduces $\alpha_{zl}$ (increasing camber) over bulk of the blade span returning to the reference value at the tip. In comparing the two cruise cases, over the outboard section, there is significant reduction in camber in the 400 knots design compared to the 300 knots design. This is because at 400 knots the rotor is operating at a relatively higher effective Mach number than it is at 300 knots. Therefore, the reduction in camber is necessary to ensure that the blade sections of the 400 knots rotor operate below $M_{dd}$ to avoid large drag penalties.
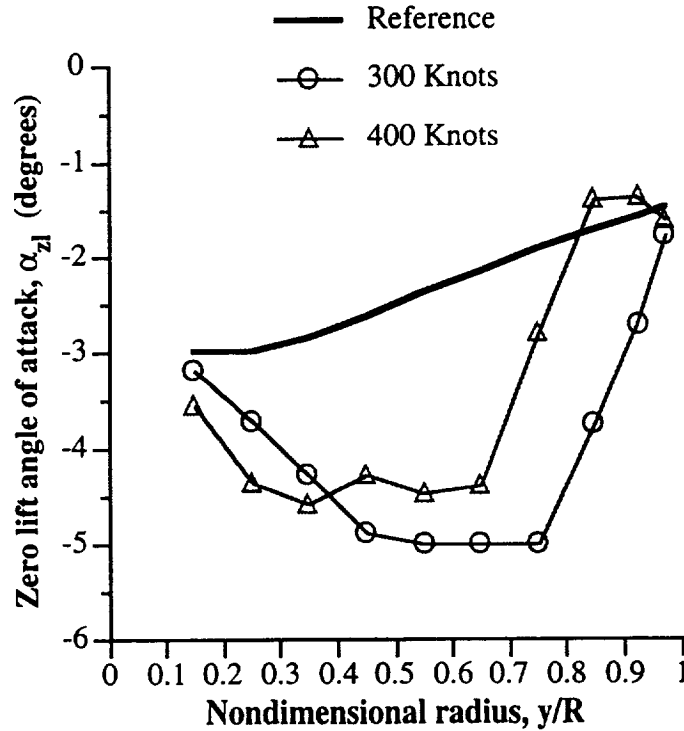


Figure 18  Zero lift angle of attack distributions

The thickness to chord ratio (t/c) distributions for the reference and the optimum rotors are shown in Fig. 19. The distributions are similar in both the 300 and the 400 knots cases at inboard and midspan sections. In both cases, significant reductions occur throughout the blade span. Such reductions in the t/c ratio are the result of an effort to increase $M_{dd}$ which is accomplished primarily through thinner airfoils. The root value of t/c is slightly higher in case of the 400 knots

rotor, compared to the rotor with a cruise speed of 300 knots. This anomaly can only be explained by noting that since the lift is so small at this location for both hover and cruise (Figs. 14 and 16), sensitivities to changes at the root are very small and therefore their effect on rotor performance in either flight condition is minimal. The tip values of the thickness to chord ratio are slightly decreased in case of the rotor operating at 400 knots forward speed, compared to the 300 knots case, due to the fact that the drag divergence Mach number must be significantly increased at these locations to ensure that the they are above the elemental Mach number.
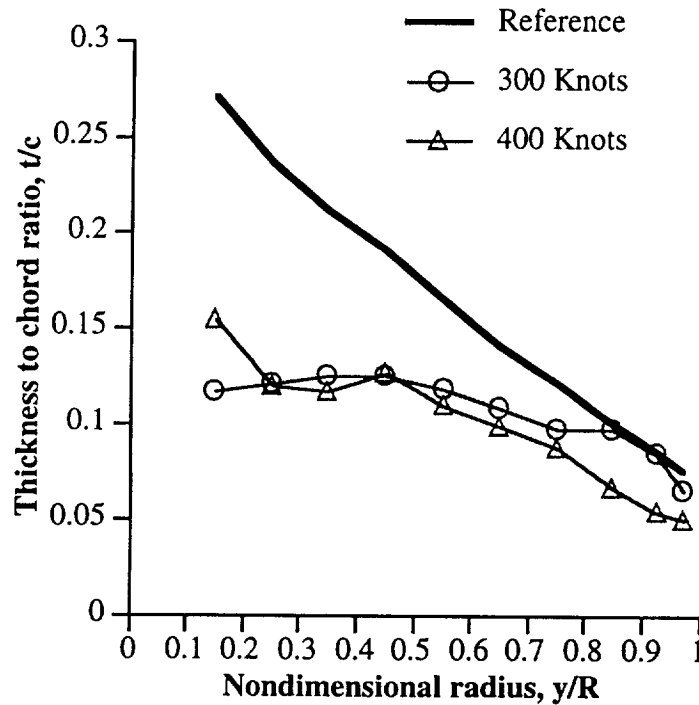


Figure 19  Thickness distributions

Off-design studies for the hover figure of merit and the high speed cruise propulsive efficiency are shown in Figs. 20 and 21.  Figure 20 illustrates that the hover figure of merit remains reasonably high over small increases in the coefficient of thrust ($C_T$). The performance is better in the 400 knots multiobjective design case.  It is interesting to note from Fig. 21 that the multiobjective designs at both 300 and 400 knots maintain reasonable values of $\eta_c$ at high off-design values of $C_T$. The efficiency drops down drastically at higher $C_T$ values in the 300 knots cruise-only optimization case.  This can be explained by the fact that in this case, the propulsive

efficiency is increased during optimization by trimming to values very near blade stall in an effort to increase the lift-to-drag ratio of the airfoil. As a result, as the thrust is increased, a greater collective pitch is required which causes the blade to stall. This is caused by the unrealistic chord distribution near the root in this case.

To summarize, the procedure developed shows the adequacy of the optimization technique in providing important design trends and trade-offs associated with improving aerodynamic efficiency in cruise and in hover sequentially as well as simultaneously. The procedure will serve as a first level in a multilevel optimization procedure. Therefore, the numerical results presented in this paper, purely obtained using performance criteria, are expected to change as other disciplines are integrated. For example, the high camber which results in high L/D ratios can also lead to high pitching moments. This problem can be addressed by combining structural and dynamic design criteria in the optimization procedure.
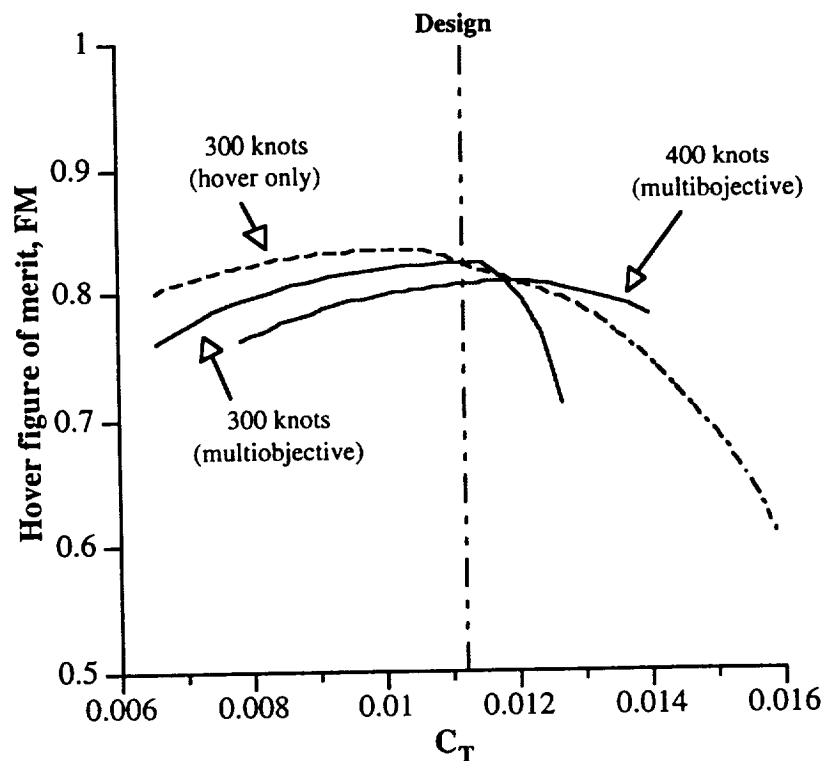
Figure 20  Hover figure of merit off-design study
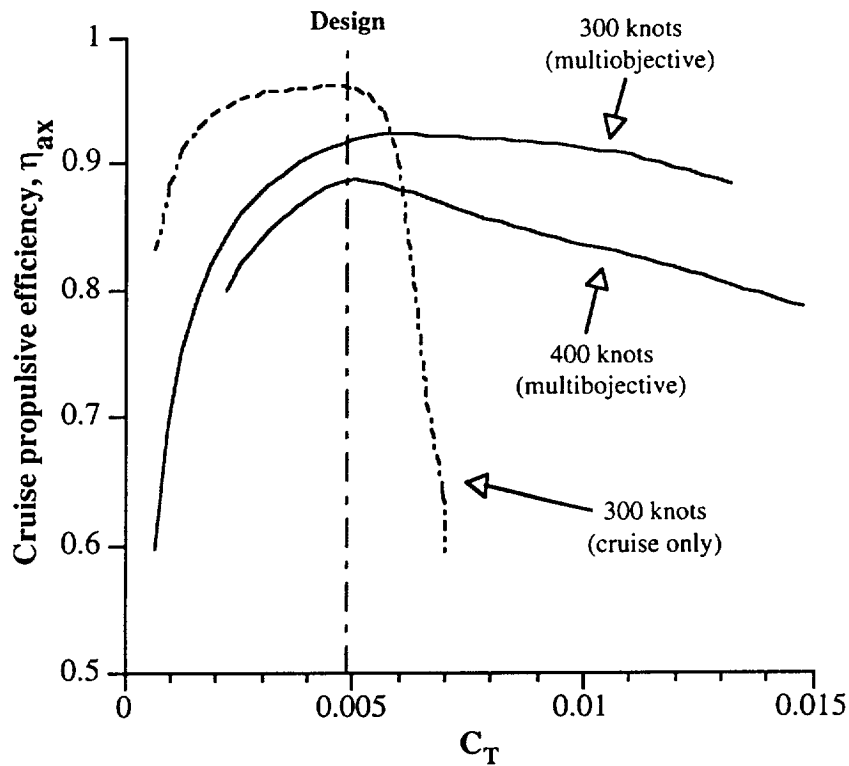
Figure 21  High speed cruise propulsive efficiency off-design study

## 3.7 Concluding Remarks

A performance based optimization procedure is developed to investigate the selection of blade aerodynamic characteristics for improving propulsive efficiency in high speed cruise as well as the figure of merit in hover.  The classical blade element momentum approach is used for the aerodynamic analysis.  The code includes an empirical correction to two dimensional stall behavior in order to represent the high lift capability of rotors and propellers.  The computational ease offered by the code allows for several design optimization problems to be studied and the subsequent trade-offs investigated.  Several different flight conditions and optimization problems are considered.  The following important observations are made.

1.  Maximum improvements in aerodynamic performance were obtained from the single objective function optimization procedures.  The optimization algorithm converged to the well known classical optimum solutions for hover and propellers.  The multiobjective function case

demonstrated the trade-offs associated with the conflicting requirements of the two flight conditions.

2. Improvements were made in the hover figure of merit and cruise propulsive efficiency in all cases and at both 300 and 400 knots. The improvements at 400 knots were not as significant due to the more demanding cruise requirements at this speed. The aerodynamic performance in this case was similar to the performance obtained in the 300 knot case, which was achieved through the proper tailoring of the blade spanwise properties.

3. The changes in the thickness and camber distributions of the optimum rotors represented an effort to increase the drag divergence Mach number without degradation of the blade lifting characteristics. The rotor operating at a forward speed of 400 knots required less camber than the 300 knots rotor in order to achieve the higher drag divergence Mach numbers necessary to remain above elemental Mach numbers.

# 4. Coupled Aerodynamic and Structures Optimization

For this objective, the aerodynamic and structural design criteria in both high speed cruise and in hover are addressed by developing a multilevel decomposition based optimization procedure. At the upper level, the aerodynamic performance of prop-rotors is optimized for both high speed cruise and hover using planform variables. Constraints are imposed on the rotor thrust in hover and in cruise. At the lower level, the rotor is optimized for improved structural performance using composite ply orientations as design variables. Since the lower level optimization involves discrete design variables, an optimization procedure, based on simulated annealing technique [14], is developed to address this complex problem. The results of the optimization procedure are compared with the same reference rotor used in the first objective (Chapter 3).

For the aerodynamics analysis, the same algorithm used in the aerodynamic optimization objective (Chapter 3) is used. The procedure offers a significant reduction in computational effort from more comprehensive procedures which were previously used by Chattopadhyay and McCarthy [4,5,15-17] as demonstrated in the first objective of this report. The use of this analysis within an optimization procedure also provides realistic design trends as demonstrated by McCarthy et al. [18]. The structural analysis is performed using a composite box beam model which includes blade pre-twist, taper and sweep to represent the principal load carrying member in the blade. In this research, a quasi one-dimensional composite beam theory, based on the model developed by Smith and Chopra [19], is extended to include beam pre-twist, taper and spanwise sweep. The procedure offers significant computational savings from more refined finite element models while maintaining sufficient accuracy.

## 4.1 Multilevel Optimization Problem

Multidisciplinary design optimization of rotary wing aircraft can be a computationally intensive task if all of the disciplines involved are coupled with the optimizer and the optimization is performed "all-at-once" in a single level. Decomposition techniques, through which such complex optimization problems can be reduced into a number of sub problems, can be very effective in

26

addressing this issue. Very recently, such techniques have been applied to rotary wing optimization problems [20,21]. In this paper, the multilevel decomposition procedure is used to address the complex multidisciplinary issues associated with high speed prop-rotor design. The optimization procedure is decomposed into two levels. At the upper level the aerodynamic performance is improved and at the lower level, the objective is to improve the structural performance of the blade using composite tailoring. The upper and lower levels are coupled through the use of optimal sensitivity parameters [21], which are essential in maintaining proper coupling between the levels. Following is a description of the decomposition and the optimization problem formulation.

### 4.1.1 Upper Level

At this level, the axial efficiency in high speed cruise ($\eta_c$) and the hover figure of merit (FM) are maximized simultaneously. Constraints are imposed on the physical dimensions of the blade to ensure that the load carrying member of the rotor is maintained within the dimensions of the airfoil. The blade is discretized and design variables include the values of the chord (c), twist ($\theta$), thickness to chord ratio (t/c), zero lift angle of attack ($\alpha_{zl}$) at each node. The sweep distribution, however, is not discretized in order to ensure continuity of the elastic axis. The lifting line is assumed to be a quadratic function of the following form.

$$x_{a/c} = d_1 x + d_2 (4y^2 - 3y) \tag{10}$$

where $x_{a/c}$ is the position of the aerodynamic center measured from the leading edge of the chord. The aerodynamic center is assumed to coincide with the elastic axis of the load carrying structural member used in the problem formulation. The coefficients which determine the position of the aerodynamic center, $d_1$ and $d_2$, are used as design variables. Note that the functions associated with these coefficients ($f_1(y) = y$ and $f_2(y) = 4y^2 - 3y$) are orthogonal to each other which is a favorable characteristic for optimization. The sweep distribution can then be formulated using this expression as follows.

$$\Lambda(y) \quad = \quad \tan^{-1}(dx/dy)$$

$$= \quad \tan^{-1}\{d_1 + d_2(8y - 3)\} \tag{11}$$

The optimization problem is stated as follows.

Maximize    $FM(\Phi), \eta_c(\Phi)$

subject to    $T_h = (T_h)_{ref}$

$T_c = (T_c)_{ref}$

$\kappa t_{hor} \le t_{max}$

where $\Phi = [c(y), \theta(y), \Lambda(y), \alpha_{zl}(y), t/c(y)]$ is the design variable vector. The quantity $t_{hor}$ is the thickness of the horizontal wall in the box beam, $t_{max}$ is the maximum thickness of the airfoil and $\kappa$ is a scaling factor used to ensure that the box beam is maintained within the airfoil cross section. Since the optimization problem involves more than one design objective, the problem is formulated using the Kreisselmeier-Steinhauser (K-S) function approach (Chapter 3).

### 4.1.2 Lower Level

The objective at this level is to minimize the tip displacements in hover and in cruise. The most critical displacements in hover are the vertical displacement ($w_h$) and the elastic twist ($\phi_h$). In cruise, the elastic twist ($\phi_c$) and the inplane displacement ($v_c$) are important. Therefore, these four displacements are selected as the individual objective functions to be minimized. Ply orientations are used as design variables. However, to avoid impractical orientations, the ply angles are chosen from a set of standard values $[0°, \pm 15°, \pm 30°, \ldots, 90°]$. The Tsai-Wu failure criterion [22] is used, which assumes that to avoid material failure the following equation representing a failure surface in stress-space must be satisfied.

$$\left(\frac{1}{\sigma_{1_T}} - \frac{1}{\sigma_{1_C}}\right)\sigma_1 + \left(\frac{1}{\sigma_{2_T}} - \frac{1}{\sigma_{2_C}}\right)\sigma_2 + \frac{\sigma_1^2}{\sigma_{1_T}\sigma_{1_C}} - \frac{\sigma_1\sigma_2}{\sqrt{\sigma_{1_T}\sigma_{1_C}\sigma_{2_T}\sigma_{2_C}}} + \frac{\sigma_2^2}{\sigma_{2_T}\sigma_{2_C}} + \frac{\tau_{12}^2}{\tau_{12_s}^2} < 0 \tag{12}$$

where $\sigma_1$ and $\sigma_2$ represent normal stresses along the material axes and $\tau_{12}$ represents the shear stress (see Fig. 22). The subscripts (T), (C) and (s) represent the ultimate stress in tension,

compression and shear, respectively. This reduces the total number of constraints as individual constraints on the stress ($\sigma_1$, $\sigma_2$ and $\tau_{12}$) at each ply are avoided. Each of the composite plates used in the box beam modeling are assumed to be symmetric about the midplane of the plate and the beam itself is assumed to be symmetric about its local axes, $\eta$ and $\zeta$ (Fig. 23). Therefore, the above failure criterion is imposed, on each lamina, at each of the four corners of the box beam to prevent failure due to stresses.
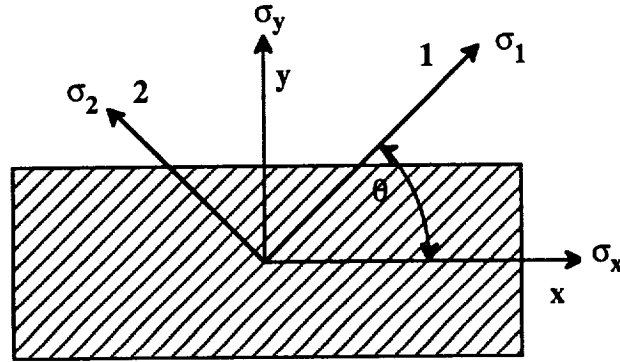


Figure 22  Composite lamina material axes
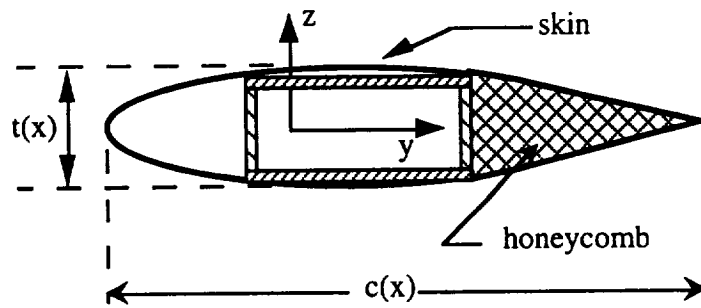


Figure 23  Blade cross section

## 4.2 Analysis

### 4.2.1 Aerodynamic Analysis

The aerodynamic formulation is based on the model used in the aerodynamic optimization objective. Further details of this analytical technique are found in Chapter 3 and Ref. 18. The aerodynamic analysis is coupled with a structural analysis which is described next. Therefore, the

results of the complete analysis represent trimmed static solutions which include the effects of elastic deformations.
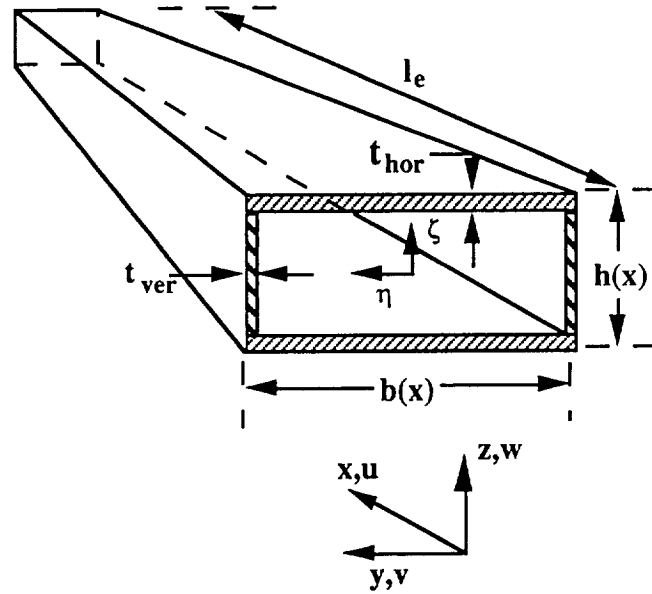


Figure 24 Composite box beam

### 4.2.2 Structural Analysis

The load carrying member of the rotor is modeled as a single cell composite box beam (Figs. 23 and 24). In addition to the structural member inside the airfoil, the weights of the honeycomb structure and the blade skin are also included in the total weight calculation. The blade is discretized using finite elements with 19 total degrees of freedom, $U_e$, and unequal element sizes. Using the finite element model it is possible to incorporate blade pre-twist and sweep distributions into the problem formulation. The nodal degrees of freedom are described as follows.

$$U_e^T = [u_1, u_2, u_3, u_4, v_{b_1}, v'_{b_1}, v_{b_2}, v'_{b_2}, w_{b_1}, w'_{b_1}, w_{b_2}, w'_{b_2}, \phi_1, \phi_2, \phi_3, v_{s_1}, v_{s_2}, w_{s_1}, w_{s_2}] \qquad (13)$$

where u is the axial displacement, v and w are the inplane horizontal and vertical displacements and $\phi$ is the elastic twist. First partial derivatives with respect to the spanwise axis (x) are denoted ( ′ ). The formulation assumes that the inplane displacements can be decoupled into a term corresponding to pure bending and a term corresponding to shear as shown below.

$$v = v_b + v_s \tag{14}$$

$$w = w_b + w_s \tag{15}$$

where the subscript (b) refers to the displacement due to beam bending and the subscript (s) refers to the displacements due to shear. Identical node locations are used in specifying both aerodynamic and structural parameters.

The outer dimensions of the box beam (Fig. 24) are constant percentages of the chord and thickness. Each composite plate used to model the composite box beam is assumed to be symmetric about the midplane of the plate. Each plate is made up of 24 laminated orthotropic composite plies. Further, the box beam is assumed to have double symmetry about the local coordinate axes ($\eta$ and $\zeta$). This ensures that the two vertical walls are identical to each other and also that the two horizontal walls are identical. The vertical and horizontal walls, however, are assumed to be independent of each other. The beam cross section is described by stretching, bending, twisting, shearing and torsion related warping. The stress-strain ($\sigma$ - $\varepsilon$) relationships in the vertical and horizontal walls are written as follows.

$$\begin{Bmatrix} \sigma_{xx} \\ \sigma_{\varsigma\varsigma} \\ \sigma_{x\varsigma} \end{Bmatrix}_v = \begin{bmatrix} \overline{Q}_{11} & \overline{Q}_{12} & \overline{Q}_{16} \\ \overline{Q}_{12} & \overline{Q}_{22} & \overline{Q}_{26} \\ \overline{Q}_{16} & \overline{Q}_{26} & \overline{Q}_{66} \end{bmatrix}_v \begin{Bmatrix} \varepsilon_{xx} \\ \varepsilon_{\varsigma\varsigma} \\ \varepsilon_{x\varsigma} \end{Bmatrix}_v \tag{16}$$

$$\begin{Bmatrix} \sigma_{xx} \\ \sigma_{\eta\eta} \\ \sigma_{x\eta} \end{Bmatrix}_h = \begin{bmatrix} \overline{Q}_{11} & \overline{Q}_{12} & \overline{Q}_{16} \\ \overline{Q}_{12} & \overline{Q}_{22} & \overline{Q}_{26} \\ \overline{Q}_{16} & \overline{Q}_{26} & \overline{Q}_{66} \end{bmatrix}_h \begin{Bmatrix} \varepsilon_{xx} \\ \varepsilon_{\eta\eta} \\ \varepsilon_{x\eta} \end{Bmatrix}_h \tag{17}$$

where the subscripts (v) and (h) indicate vertical and horizontal walls, respectively. The off-axis stiffness matrix for each lamina is denoted $\overline{Q}_{ij}$ (i, j = 1,2 & 6). The strains in the vertical walls are expressed as follows.

$$\varepsilon_{xx} = u' - \eta(v'' - \gamma_{\chi\eta}') - \zeta(w'' - \gamma_{\chi\zeta}') - \lambda_w \phi'' \tag{18}$$

$$\varepsilon_{x\zeta} = \left(\eta - \frac{\partial \lambda_w}{\partial \zeta}\right)\phi' + \gamma_{\chi\zeta} \tag{19}$$

$$\varepsilon_{\zeta\zeta} = a_0 u' + b_1\eta(v'' - \overset{\circ}{\gamma}_{\chi\eta}{}') - c_2\zeta(w'' - \gamma_{\chi\zeta}{}') - (d_0 + d_1\eta + d_2\zeta)\phi'$$

$$+ (f_0 + f_2\zeta)\overset{\circ}{\gamma}_{\chi\eta} + (g_0 + g_1)\gamma_{\chi\zeta} \tag{20}$$

where u is the axial displacement, v and w are the horizontal and vertical inplane displacements, respectively, $\phi$ is the twist angle and $\overset{\circ}{\gamma}_{\chi\eta}$ and $\gamma_{\chi\zeta}$ represent the inplane shear stresses (Fig. 24). The superscript ( $''$ ) represents second partial derivatives with respect to x. Similar expressions are obtained for the horizontal walls. The out-of-plane warping is denoted $\lambda_w$ and the coefficients $a_0$ - $g_1$ are determined such that the net inplane forces and moments in the horizontal and vertical walls are zero. Using these conditions, the equations of equilibrium are written as follows.

$$\begin{Bmatrix} F \\ Q_y \\ Q_z \end{Bmatrix} = \begin{bmatrix} k_{11} & 0 & k_{13} \\ 0 & k_{22} & k_{23} \\ k_{13} & k_{23} & k_{33} \end{bmatrix} \begin{Bmatrix} u' \\ \gamma_{x\eta}^{o} \\ \gamma_{x\zeta}^{o} \end{Bmatrix} \tag{21}$$

$$\begin{Bmatrix} T \\ M_y \\ M_z \end{Bmatrix} = \begin{bmatrix} k_{44} & 0 & k_{46} \\ 0 & k_{55} & k_{56} \\ k_{46} & k_{56} & k_{66} \end{bmatrix} \begin{Bmatrix} \phi' \\ w'' - \gamma_{x\zeta}^{o}{}' \\ v'' - \gamma_{x\eta}^{o}{}' \end{Bmatrix} \tag{22}$$

where $M_z$ and $M_y$ are the lagging and flapping moments, respectively and T is the torsional moment. The axial force is denoted F, the inplane horizontal and vertical shear forces are denoted $Q_y$ and $Q_z$, respectively and $k_{ij}$ (i, j = 1, 2, ... , 6) represent the stiffness matrix elements. Further details of the formulation can be found in Ref. [19].

The elemental equilibrium equations are written in vector form as follows.

$$\mathbf{F_e} = \mathbf{K_e u_e} \tag{23}$$

where $\mathbf{F_e} = [F \ Q_y \ Q_z \ T \ m_x \ m_z]^T$ is the elemental force vector, $\mathbf{K_e} = [k_{ij}]$ is the elemental stiffness matrix and $\mathbf{u_e} = [u' \ \gamma_{\chi\eta} \ \gamma_{\chi\zeta} \ \phi' \ (v'' - \gamma_{\chi\eta}{}') \ (w'' - \gamma_{\chi\zeta}{}')]^T$ represents the elemental degrees of freedom in the local coordinate system. Using these principles a finite element approach is developed using the weak formulation as follows.

$$\int_{o}^{R} H_G F_G dx = \int_{o}^{R} H_G K_G H_G U_G dx \qquad (24)$$

where $F_G$ and $K_G$ are the global force vector and stiffness matrix, respectively, $U_G$ is the global vector of discrete nodal degrees of freedom and $H_G$ is the global representation of the interpolation matrix. The blade displacements are written in the discretized elemental form as shown below.

$$u(s) = H(s)U_e \qquad (25)$$

where $H(s)$ represents the complete set of interpolation vectors and $U_e$ is the elemental nodal displacement vector (Eqn. 13).

## 4.3 Optimization Implementation

The multilevel optimization technique used in this research decomposes the design problem into a level where only continuous design variables are used (upper level) and a second level where discrete design variables are used (lower level). Therefore, two separate optimization strategies are necessary. Since traditional optimization techniques minimize only a single objective function, it is necessary to transform the original objective functions, at each level, using multiobjective function techniques. The technique used for each level is the Kreisselmeier-Steinhauser (K-S) function approach. A nonlinear programming procedure (NLP) based on the Davidon-Fletcher-Powell method (DFP) is used as the optimization algorithm at this level [23]. For the lower level, an optimization procedure has been developed based on the method of simulated annealing [10] which is described next.

If ply angles are used as continuous design variables and are later rounded off to the nearest practical value (e.g. 47.3° being rounded off to 45°), the result can lead to sub optimal designs [24]. Allowing the ply angles to vary within a set of prescribed values during optimization is a more efficient approach. Therefore, in the structural optimization problem, the plies are selected from within a set of pre-selected orientations of integer multiples of ±15° such as 0°, ±15°, ±30°, ..., 90°. This reduces the problem into a discrete optimization problem and conventional gradient

33

based optimization procedures are no longer applicable. Using the procedure developed in the current work, the optimization problem is transformed into a completely discrete problem. The new discrete problem can now be optimized using a simulated annealing technique which has been shown to be effective in a variety of different engineering applications [25-27]. The procedure developed is outlined below.

The multiobjective optimization problem is stated as follows:

$$\text{Minimize} \quad F_K(a_i) \qquad K = 1, 2, ..., NF$$

$$\text{subject to} \quad g_M(a_i) \qquad M = 1, 2, ..., NC$$

$$i = 1, 2, ..., NDV$$

where NF is the number of objective functions, NC is the number of constraints, NDV is the number of design variables and **a** is the vector of design variables. The $i^{th}$ design variable can assume any value from the design variables vector of pre-selected values, $d_{iq}$ such as $0°$, $\pm 15°$, $\pm 30°$, ... , $90°$ for ply angles. Therefore, the objective functions and constraints are completely represented by discrete design variables. The multiobjective optimization problem is transformed into a single unconstrained composite function to be minimized using the K-S function approach as previously described. An optimal solution cannot be guaranteed for a discrete optimization problem without evaluating every possible combination of discrete variables which is computationally impractical. Near optimal solutions can be obtained, however, with significant improvements in all objective functions with a reasonable amount of computational effort.

The simulated annealing algorithm is described briefly as follows.

*START*
*Current design is F*
*Perturb current design $F_{new}$*
*If $F_{new} \leq F$ then*
    *$F = F_{new}$*
*Else if $p_{acc} \geq p$ then*
    *$F = F_{new}$*
*End if*
*Go to START*

34

where F is the objective function to be minimized and p is a random number such that $0 \leq p \leq 1$. The acceptance probability $p_{acc}$ of retaining a worse design is computed as follows.

$$p_{acc} = \exp\left(-\frac{\Delta F}{T_k}\right) \tag{26}$$

where $\Delta F$ is the change in the objective function and $T_k$ is the "temperature" which is reduced during successive iterations, to ensure smooth convergence, according to:

$$T_k = (r_c)^k T_0 \tag{27}$$

where $T_0$ is the initial temperature and $r_c$ is the cooling rate which determines the temperature at the $k^{th}$ iteration. This reduces the probability of accepting a worse design. Occasionally accepting a worse design under the given probability allows the algorithm to climb out of possible local minima. The above loop is repeated a prescribed number of times for each cycle in the multilevel optimization procedure.

### 4.4 Results

The reference rotor used is the same representation of the XV-15 prop-rotor which was used in the aerodynamic optimization objective. Identical flight conditions are used which are summarized in Table 1. The blade is discretized into 10 segments (11 node points). The composite material used in the structural analysis is carbon-PEEK AS4/APC2 [28] (Table 2).

At the upper level the design variables for the chord (c), twist ($\theta$), zero angle of attack ($\alpha_{zl}$) and thickness to chord ratio (t/c) are all based on discrete nodal values whereas the sweep distribution ($\Lambda$) is assumed to be based on a quadratic lifting line. This yields a total of 46 design variables. The scaling factor ($\kappa$), used in the upper level constraints to ensure that the box beam is maintained in the airfoil, is assumed to vary as follows.

$$\kappa = \begin{cases} 4.0 & \bar{y} < 0.8 \\ 3.0 & 0.8 \leq \bar{y} < 0.95 \\ 2.5 & 0.95 \leq \bar{y} \leq 1.0 \end{cases} \tag{28}$$

where $\bar{y}$ is the nondimensional radial location. The reason for this variation is to ensure the validity of thin wall theory at inboard sections of the blade, since the majority of the load is carried in this section, without being too restrictive at the tip where thinner airfoils can improve the aerodynamic performance. The tolerance on the lower level objective functions, used as optimal sensitivity parameters at this level, is initially 5 percent. This value is reduced to 0.5 percent after 6 complete multilevel cycles in order to ensure that there is very little degradation of lower level objective functions at the upper level. A nonlinear programming technique based on the DFP algorithm, developed at Arizona State University, is used for optimization at this level.

Table 2  Composite properties

| | Carbon-PEEK  AS4/APC2 | |
|---|---|---|
| $E_1$ | 19.43 | $(10^6)$ p.s.i. |
| $E_2$ | 1.29 | $(10^6)$ p.s.i. |
| $G_{12}$ | 0.74 | $(10^6)$ p.s.i. |
| $\nu_{12}$ | 0.28 | |
| $\sigma_{1T}$ | 309. | $(10^3)$ p.s.i. |
| $\sigma_{1C}$ | 160. | $(10^3)$ p.s.i. |
| $\sigma_{2T}$ | 11.6 | $(10^3)$ p.s.i. |
| $\sigma_{2C}$ | 29.0 | $(10^3)$ p.s.i. |
| $\tau_{12s}$ | 23.2 | $(10^3)$ p.s.i. |

At the lower level, the discrete values of the ply orientations are used as design variables. Since a symmetric and balanced lay-up is used in both the vertical and horizontal walls, this leads to 12 independent design variables which can assume any of the 7 pre-selected values of ply angle orientations. The design space associated with this problem therefore consists of nearly 14 billion ($7^{12}$) possible combinations. The actual number of loops used at each multilevel cycle is 1000 iterations which represents only a very small portion of the total design space. The value of the K-S function multiplier ($\delta$) used at this level is initially set to 5.0, but is subsequently reduced to 1.0 after 4 multilevel iterations. This is done to increase the sensitivity of the K-S function to changes in all of the objective functions and constraints. The cooling rate ($r_c$) used in the simulated annealing algorithm is 0.995 and the initial temperature ($T_0$) is set to 1.0.

Convergence of the multilevel optimization procedure is achieved in 7 cycles, where a cycle represents an individually converged optimization including both upper and lower levels. The initial design used in this optimization procedure corresponds to the optimal results obtained from a purely aerodynamic optimization using the same aerodynamic analysis (Chapter 3) [18]. The results from the multilevel based optimization are compared to the design obtained from the purely aerodynamic optimization and also to a reference rotor which represents the original XV-15 prop-rotor. The results are presented in Table 3 and Figs. 25-33.

The upper level objective functions are presented in Fig. 25. It is shown in the figure that the hover figure of merit (FM), which is increased by 6.6 percent in the purely aerodynamic procedure, is further increased in the multilevel optimization (7.5 percent) compared to the reference rotor. The propulsive efficiency in high speed cruise ($\eta_c$) is increased by 3.6 percent from the reference rotor in the aerodynamic formulation and in the multilevel procedure the increase is slightly less (3.2 percent). These trends can be explained by examining the rotor planform.
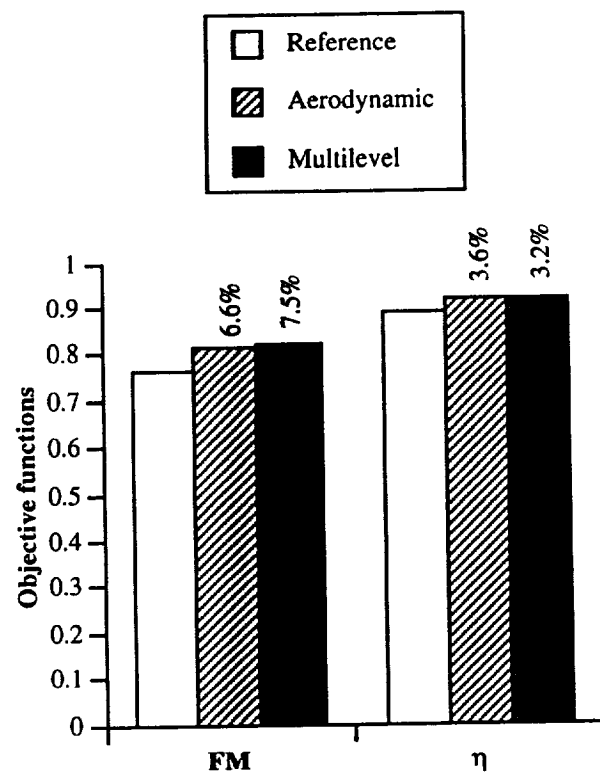


Figure 25  Summary of upper level objective functions

37

The optimum and reference chord distributions (c) are shown in Fig. 26 where it is observed that the planforms obtained from both the aerodynamic and the multilevel optimization procedures are similar in shape and they differ sharply from the reference chord distribution. The optimum distributions closely resemble the well known ideal hover planform. Such a distribution is the result of the large solidity requirement necessary to achieve the required thrust in hover. The reduction in the outboard section, relative to the reference rotor, is attributable to the lack of any maneuver margin requirement in the optimization problem formulation.
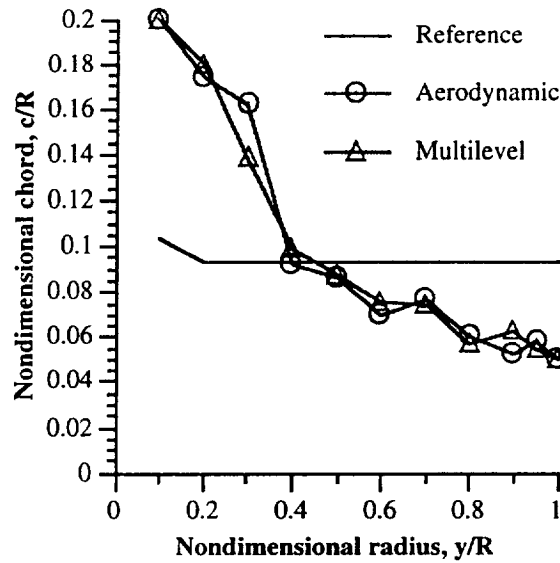


Figure 26  Chord distributions

Figure 27 shows the thickness to chord ratio (t/c) distributions for the three rotor configurations. From the figure, it is seen that there are large reductions from the reference rotor at the inboard sections in both of the optimum rotors. In case of the purely aerodynamic formulation, the optimum thickness is reduced from the reference blade throughout the blade span except at the 90 percent span location. This decrease represents an attempt to improve the rotor performance by reducing the profile drag. In case of the multilevel optimization procedure, similar trends are noted, only the reductions from the reference rotor are not as large. In fact, at the outboard section the airfoil thickness is actually increased from the reference values. The reason for these increases at the tip are to satisfy the constraint which ensures that the box beam can be contained within the

38

airfoil. In case of the aerodynamic procedure, these constraints are violated at the tip. Since the multilevel procedure results in a thicker blade, compared to that from the aerodynamic optimization, the maximum coefficient of lift ($C_{L_{max}}$) is increased in this design. This increase in $C_{L_{max}}$ subsequently improves the hover figure of merit which explains the slight increase in FM from aerodynamic formulation. However, associated with the thicker airfoils are lower drag divergence Mach numbers ($M_{dd}$) which cause the high speed cruise performance to be slightly diminished, from the purely aerodynamic formulation.
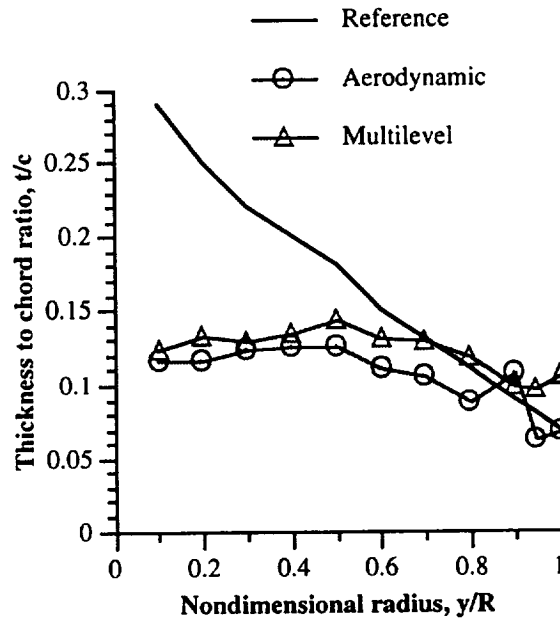


Figure 27  Thickness to chord ratio distributions

The lifting line ($x_{a/c}$) and sweep ($\Lambda$) distributions for the multilevel optimization and the reference rotor are presented in Figs. 28 and 29. Note that in the purely aerodynamic formulation no sweep modeling is included. As is shown in Fig. 28, the lifting line is swept slightly forward, with the maximum offset at the tip. This results in the near linear distribution of the sweep. This sweep distribution has the effect of increasing the torsional moment about the hub in an effort to reduce the elastic twist, which in this case is negative (nose down). It must be noted that to investigate the effect of forward sweep, which can have an adverse affect on aeroelastic stability, a more comprehensive formulation including dynamic loads would have to be used.

39

The twist ($\theta$) and the zero lift angle of attack ($\alpha_{zl}$) distributions are shown in Figs. 30 and 31. From Fig. 30 it is seen that the twist distribution for the aerodynamic and the multilevel optimization results are nearly identical varying only slightly from the reference distribution. The variations are most notable at the midspan locations where the optimum twist, through this region, is more linear than the reference rotor. This is due to the high speed cruise requirements where more linear twist distributions are expected due to the high inflow velocity in forward flight. Figure 31 shows that the $\alpha_{zl}$ distributions for both the aerodynamic and the multilevel optimization procedures are nearly identical. However, in this case, both of these distributions vary drastically from the reference distribution. The figure shows that the optimum distributions are decreased significantly from the reference values at the inboard and midspan locations. This effectively increases the camber of the airfoil which improves the airfoil lift-to-drag ratio thereby improving performance. The zero lift angle of attack is then reduced (less camber) at the outboard section and is increased at the blade tip. This can be explained as the optimizer's attempt to avoid the reduction of $M_{dd}$ to values below the operational Mach number at this location.
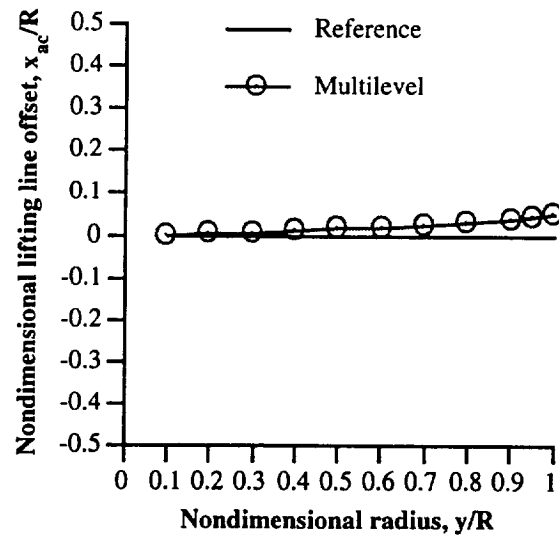
Figure 28  Lifting line distributions
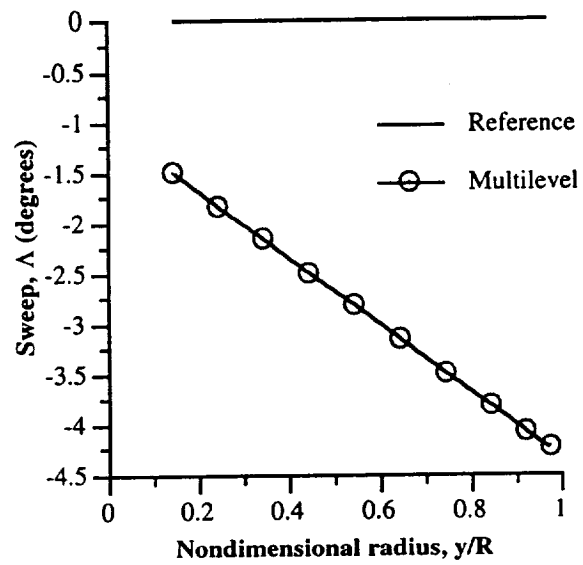
Figure 29  Blade sweep distributions
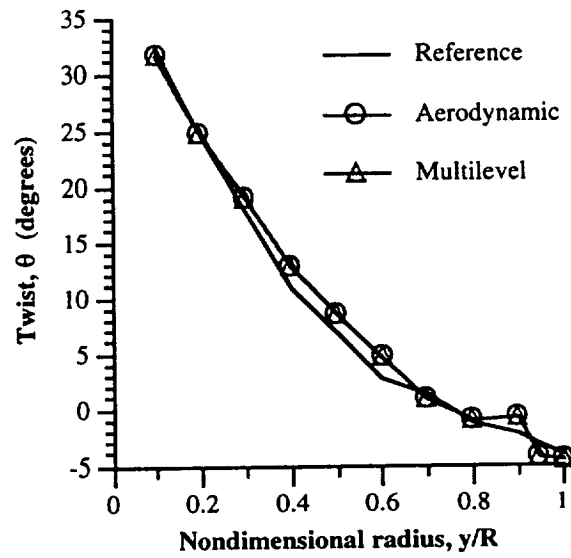


Figure 30  Blade twist distributions

41
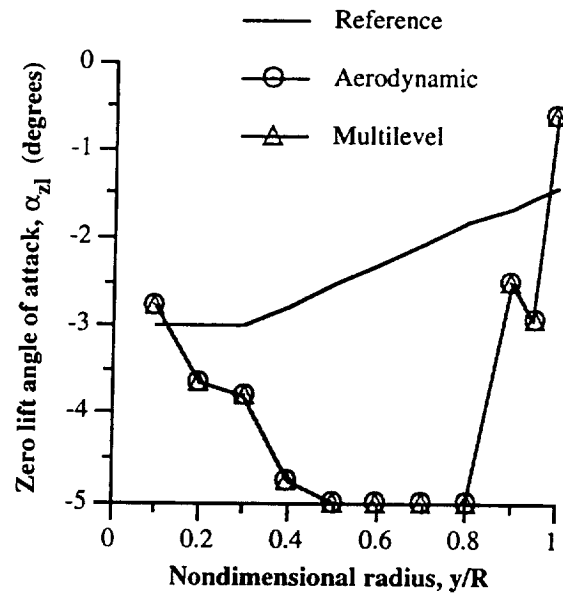
Figure 31  Zero lift angle of attack distributions

The nondimensional values of the lower level objective functions are presented in Fig. 32 where large deviations from the reference rotor are observed in the purely aerodynamic and multilevel optimization procedures. It should be noted here that the purely aerodynamic results were obtained in Ref. 18 (Chapter 3) without any structural considerations. The structural performance results pertaining to that case, which are presented here, are computed using the optimized rotor planform obtained from that study. In the aerodynamic formulation it is seen that the elastic twist in hover ($\phi_h$) and in cruise ($\phi_c$) and the vertical displacement in hover ($w_h$) are significantly increased by 53, 61 and 6.5 percent, respectively, from the reference rotor. However, the horizontal displacement in cruise is actually decreased by 15 percent. In case of the multilevel optimization in which these displacements are included as objective functions, it is seen that there are significant reductions in all four displacements, from reference to optimum, after optimization. In this case, the elastic twist in hover and in cruise are reduced by 9.9 and 14 percent, respectively and the vertical displacement in hover and the horizontal displacement in cruise are reduce by 16 and 3.9 percent, respectively. The magnitude of all the displacements are also reduced throughout the blade span from the reference values. An example of this is seen in Fig. 33 which displays the elastic twist deformations. This shows that in case of the multilevel

42

formulation, even though the aerodynamic performance is comparable to the purely aerodynamic design (Fig. 25), the structural performance is greatly improved. These reductions are attributable to increased thickness of the airfoil, which in turn increases the height of the box beam, and also to the improved stacking sequence.
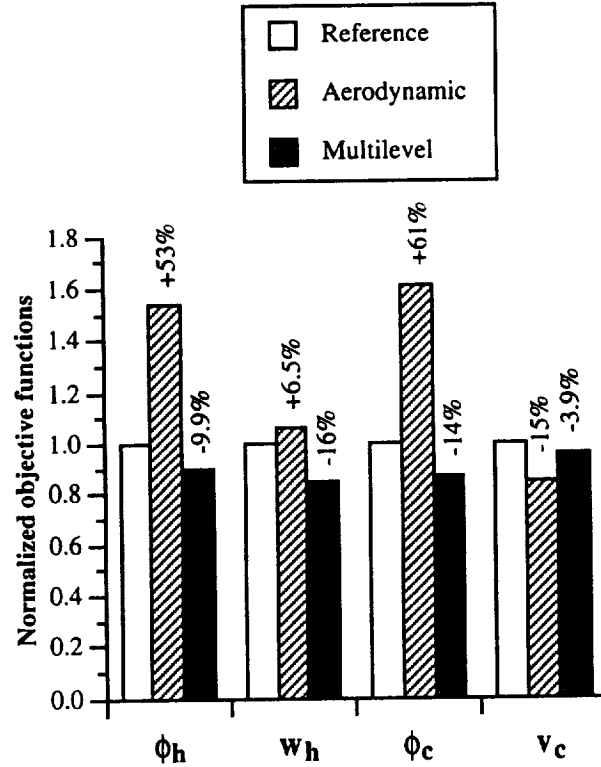


Figure 32 Summary of lower level objective functions

The composite laminate stacking sequences are presented in Table 3. Note that in the reference blade, the horizontal and vertical walls are assumed to have the same stacking sequence. Further, since all of the laminates are considered to be symmetric about their midplane, only 12 of the 24 total plies are presented in the table for each wall. The individual ply thickness used in this study is 0.001 inches which results in a total wall thickness of 0.24 in. For the sake of comparison, the structural response in case of the purely aerodynamic optimization formulation is obtained using the reference stacking sequence. Note that in the optimal configuration, there is a reduced number of ±45° plies and an increased number of ±30° plies. This can be explained as an attempt to

43

compromise between the conflicting requirements of reduced elastic twist and reduced transverse displacements.
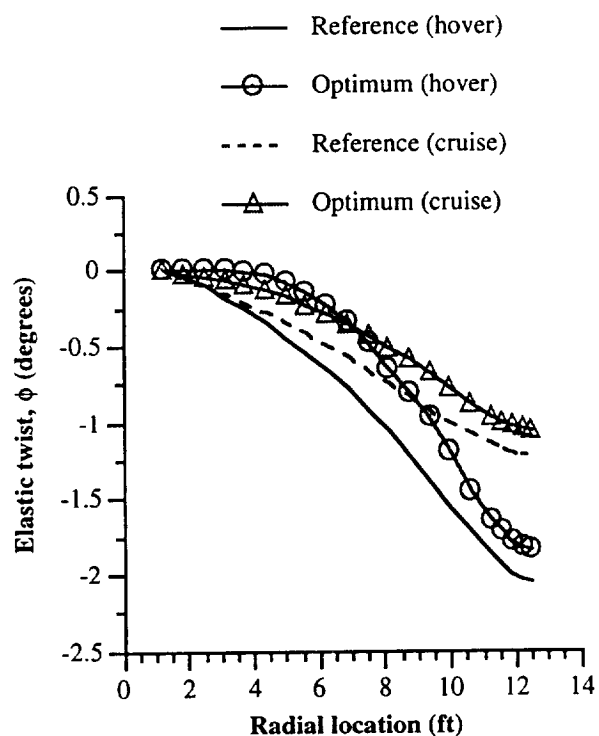


Figure 33  Elastic twist distributions

Table 3  Ply orientation angles

| Reference | | Optimum | |
|---|---|---|---|
| | | Horizontal Wall | Vertical Wall |
| Outer ply | 0° | 15° | 0° |
| | 0° | -15° | 0° |
| | 0° | 0° | 15° |
| | 0° | 0° | -15° |
| | 15° | 15° | 30° |
| | -15° | -15° | -30° |
| | 15° | 15° | 15° |
| | -15° | -15° | -15° |
| | 45° | 30° | 45° |
| | -45° | -30° | -45° |
| | 45° | 30° | 15° |
| midplane | -45° | -30° | -15° |

44

## 4.5 Concluding Remarks

A multilevel optimization procedure based on aerodynamic and structural performance is developed for an investigation of the coupled aerodynamic and structural design problem of high speed prop-rotors. The classical blade element momentum approach is used for the aerodynamic analysis. The structural analysis is performed using a quasi one-dimensional finite element approach based on a composite box beam model. At the upper level, a nonlinear programming technique based on the Davidon-Fletcher-Powell method is used as the optimization algorithm. At the lower level, a discrete optimization based on the simulated annealing technique is used. The optimization problems are formulated using the Kreisselmeier-Steinhauser function approach. The optimum results obtained in this study are compared with a reference rotor and with a design obtained using a purely aerodynamic optimization procedure. Convergence is achieved after 147 total aerodynamic optimization cycles at the upper level and a total of 7000 simulated annealing iterations at the lower level. The following important observations are observed.

1. The multilevel optimization procedure significantly improves the aerodynamic and structural response of a high speed prop-rotor blade. Further, the aerodynamic performance is comparable to a purely aerodynamic design demonstrating the success of the decomposition based procedure.

2. The simulated annealing algorithm successfully minimizes the tip displacements by altering the composite plate stacking sequences in the horizontal and the vertical walls. The optimum composite stacking sequence represents a compromise between reduced elastic twist and reduced transverse bending. This is manifested through the selection of ±30 degree plies in both the horizontal and the vertical walls.

3. The airfoil thickness to chord ratio is increased from the purely aerodynamic formulation due to structural constraints on the blade. The thicker airfoil increases the hover performance with only a slight degradation in the cruise efficiency from the optimum aerodynamic results.

4. The optimum blade is swept slightly forward to improve the elastic twist. The sweep increases the torsional moment which has the effect of reducing the nose down elastic twist.

5. The chord, twist and zero lift angle of attack distributions differ significantly from the reference blade but are very similar to the optimum aerodynamic configuration.

6. The elastic deformations at the blade tip as well as throughout the blade span are reduced from reference values. This is achieved through a combination of an improved ply stacking sequence and slightly thicker airfoils.

# 5. Multipoint Optimization

The optimization procedure of Chapter 4 is now extended to include the take-off performance in the formulation. The aerodynamic and structural design criteria in high speed cruise, in hover and in take-off are addressed using the multilevel decomposition-based optimization procedure developed in Chapter 4. At the upper level, the aerodynamic performance of prop-rotors is optimized for each flight condition using planform variables. Constraints are imposed on the rotor thrust in all three flight conditions. A nonlinear programming technique based on the Broyden-Fletcher-Goldfarb-Shanno (BFGS) [23] algorithm is used for the optimization. At the lower level, the rotor is optimized for improved structural performance using composite ply stacking sequence as design variables. Since only discrete design variables are used at the lower level, an optimization procedure, based on simulated annealing algorithm (Chapter 4), is developed to address this complex problem.

## 5.1 Analysis

The aerodynamic and structural analyses are performed in this objective with the same formulation used in the Chapters 3 and 4. Details of these formulations can be found in those chapters.

## 5.2 Optimization Implementation

The primary objectives of this study are to improve aerodynamic and structural performance of the tilt-rotor aircraft at three design points, high speed cruise, hover and take-off. Since the problem is complex and is associated with several objectives functions, constraints and design variables, a multilevel decomposition technique is used to decompose the problem into two levels. In this study, the decomposition technique developed in Chapter 4 (Ref. 29) is used to formulate an optimization problem involving a total of three flight conditions. The optimization procedure is decomposed into two levels. The aerodynamic performance is improved at the upper level and the structural criteria are addressed at the lower level. Following is a description of the two levels.

## 5.2.1  Upper Level

The axial efficiency in high speed cruise ($\eta_c$) and the figure of merit in both hover and in take-off ($FM_h$ and $FM_t$, respectively) are maximized simultaneously in this level using aerodynamic design variables.  Constraints are imposed on the rotor thrust at each of these flight conditions.  Geometric constraints are also imposed on the physical dimensions of the blade to ensure that the load carrying member of the rotor is maintained within the dimensions of the airfoil.  The blade is discretized and design variables include the values of chord (c), twist ($\theta$), thickness to chord ratio (t/c) and zero lift angle of attack ($\alpha_{zl}$) at each node.  To ensure monotony of the sweep, the following quadratic variation is used to represent the lifting line.

$$x_{a/c} = \frac{1}{2} d_1 y^2 \tag{29}$$

where $y_{a/c}$ is the position of the aerodynamic center, which in this formulation coincides with the shear center.  The coefficient $d_1$ is used as a design variable to determine this position.  Note that this sweep formulation is slightly different from the formulation used in Chapter 4.  The sweep distribution can then be formulated using this expression as follows.

$$\Lambda(y) = \tan^{-1}(d_1 y) \tag{30}$$

This also ensures continuity of the elastic axis.  The optimization problem is stated as follows.

Maximize
$$\eta_c(\Phi),\ FM_h(\Phi),\ FM_t(\Phi)$$

subject to
$$T_c = (T_c)_{ref}$$
$$T_h = (T_h)_{ref}$$
$$T_t = (T_t)_{ref}$$
$$\kappa t_{hor} \leq t_{max}$$

where the subscript 't' refers to the take-off condition and the other subscripts are as described before.

*5.2.2 Lower Level*

The structural characteristics of the rotor are investigated at this level. The objectives are to minimize the tip displacements in cruise, in hover and in take-off. The most critical of these displacements are included in the formulation. In cruise, the elastic twist ($\phi_c$) and the inplane displacement ($v_c$) are critical. In hover and in take-off conditions, the vertical displacement ($w_h$ and $w_t$, respectively) and the elastic twist ($\phi_h$ and $\phi_t$, respectively) are significant. Therefore, these six displacements are selected as the individual objective functions to be minimized. Ply orientations are used as the discrete design variables at this level. Stress constraints are imposed and the Tsai-Wu failure criterion [22] is used to reduce the number of these constraints (see Chapter 4 for more details).

## 5.3 Optimization Implementation

The optimization strategy for this two level decomposition formulation is identical to the formulation used in Chapters 4. As before the Kreisselmeier-Steinhauser (K-S) function approach is used to formulate the multiple objective functions and the constraints into a single envelope function which is then extremized. Since only continuous design variables are used during optimization at the upper level, a nonlinear programming procedure (NLP) based on the Broyden-Fletcher-Goldfarb-Shanno (BFGS) algorithm is used. The lower level comprises only discrete design variables, therefore an optimization technique based on the simulated annealing algorithm is implemented at this level. Details of this formulation are found in Chapter 4.

## 5.4 Results

The same reference rotor is used in this study. For the hover and high speed cruise, the same operating conditions used in Chapters 3 and 4 are used. To simulate the take-off condition a load factor of 1.25 is used. Inclusion of the 12 percent down load effect, results in a take-off thrust of 9100 lb. A rotational speed of 570 RPM is used and an altitude of 6695 feet is assumed to simulate a high altitude take-off. The flight conditions are summarized in Table 4. The blade is

discretized into 10 segments. The composite material used in the structural analysis is carbon-PEEK AS4/APC2 which has properties as listed in Table 2.

At the upper level the design variables include the nodal values of the chord (c), twist ($\theta$), zero angle of attack ($\alpha_{zl}$) and thickness to chord ratio (t/c). The sweep distribution ($\Lambda$) is based on a quadratic lifting line. This yields a total of 45 design variables. The same scaling factor ($\kappa$) used in Chapter 4 is employed in this objective to ensure that the box beam is maintained within the airfoil section (Eqn. 28). The tolerance on the lower level objective functions, used as optimal sensitivity parameters at this level, is initially set at 5 percent and is later relaxed to 20 percent for the tip bending displacements. An in-house code based on the Kreisselmeier-Steinhauser (K-S) function developed at Arizona State University is used as the optimization algorithm at this level. The search direction used during optimization is based on the BFGS algorithm and the two-point exponential expansion is used to approximate the objective functions and constraints. The K-S function multiplier $\delta$ is initially set at 50 and increases during optimization to values as high as 210.

Table 4  Summary of flight conditions

| | |
|---|---|
| Vehicle weight | 13,000 lb |
| Blade radius | 12.5 |
| **Hover** | |
| Altitude | Sea level |
| Thrust, $T_h$ | 7280 lb |
| Rotational speed | 570 RPM |
| **Cruise** | |
| Altitude | 25,000 ft |
| Thrust, $T_c$ | 774 lb |
| Rotational speed | 421 RPM |
| Forward speed, $V_\infty$ | 300 knots |
| **Take-off** | |
| Altitude | 6695 ft |
| Thrust, $T_t$ | 9100 lb |
| Rotational speed | 570 RPM |

At the lower level, the design variables represent discrete values of the composite ply orientations. Since a symmetric and balanced lay-up is assumed in both the vertical and the horizontal walls, this leads to 12 independent design variables which can assume any one of the 7 pre-selected values of ply angle orientations. A value of 5 is used for $\delta$, the K-S function

50

multiplier. In the simulated annealing algorithm a value of 0.995 is used for the cooling rate, $r_c$, and the initial temperature $(T_0)$ is set to 1.0.

In the multilevel problem, a total of 150 cycles is necessary for convergence at the upper level where a cycle consists of a "converged" design based upon one real analysis and several approximate function evaluations. A total of 5000 iterations are necessary at the lower level. Total convergence, including upper and lower levels, is achieved in five cycles. The results from this multiple design point optimization are presented in Tables 5 and 6 and Figs. 34 - 41.

The upper level objective functions are presented in Table 5 and Fig. 34. The figures of merit in hover $(FM_h)$ and in take-off $(FM_t)$ are increased by 6.9 and 31 percent, respectively, from the reference values. A small increase (0.52%) is obtained in the cruise propulsive efficiency $(\eta_c)$. These trends can be explained by examining the rotor planform.

Table 5 Summary of optimum results

| | Reference | Optimum |
|---|---|---|
| **Objective functions** | | |
| *Level 1* | | |
| FM (hover) | 0.760 | 0.813 |
| $\eta_{\alpha x}$ | 0.888 | 0.893 |
| FM (take-off) | 0.617 | 0.807 |
| *Level 2* | | |
| $w_h$ (in) | 11.5 | 6.95 |
| $v_c$ (in) | -2.21 | -1.03 |
| $w_t$ (in) | 13.7 | 7.91 |
| $\phi_h$ (deg) | -2.05 | -1.77 |
| $\phi_c$ (deg) | -1.22 | -1.19 |
| $\phi_t$ (deg) | -1.73 | -1.39 |
| *Solidity* | | |
| area weighted, $\sigma$ | 0.08075 | 0.1055 |
| thrust weighted, $\sigma_t$ | 0.08913 | 0.08976 |

A comparison of the optimum and reference chord distributions (c) are shown in Fig. 35 and significant differences must be noted. The optimum distribution closely resembles the well known ideal hover planform with notable exceptions at the root and at the tip. The proximity to the hover planform is due to the large solidity necessary to achieve the thrust required in both hover and in take-off. The deviation (from ideal hover planform) at the root is a result of an upper bound of 0.2 which is imposed on the nondimensional chord (c/R) to avoid large chord sections. The deviation at the tip is due to a geometric constraint which is imposed to ensure that the box beam is maintained within the airfoil section. The reduction in the outboard section, relative to the reference rotor, is attributable to the lack of any maneuver margin requirement in the optimization problem formulation. Further, it is of interest to note that although the area-weighted solidity ($\sigma$) is increased by nearly 31 percent, the thrust weighted solidity ($\sigma_T$) is increased by only 7.1 percent (Table 5).
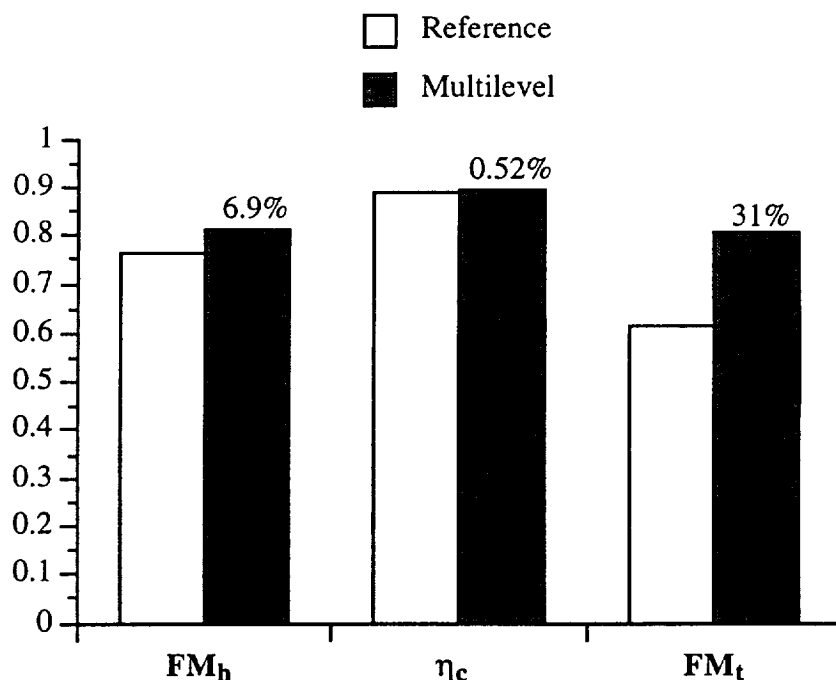


Figure 34 Summary of upper level objective functions

The thickness to chord ratio (t/c) distributions of the reference and the optimum rotor configurations are presented in Fig. 36 and show large reductions from the reference rotor at the inboard sections of the optimum rotor. The thickness is also slightly reduced from the reference

52

values at midspan locations and is slightly increased at the tip. The former is explained as an attempt to improve the rotor performance by reducing the profile drag. The latter represents the optimizer's effort to satisfy the geometric constraint which ensures that the box beam is contained within the airfoil section. Since the optimum distribution is very similar to the reference distribution at midspan locations and slight increases are observed at the tip, the profile drag over the working section of the blade in case of high speed cruise is only slightly altered. This, coupled with the chord distribution over this section of the blade, results in only a slight improvement of the high speed cruise propulsive efficiency ($\eta_c$).
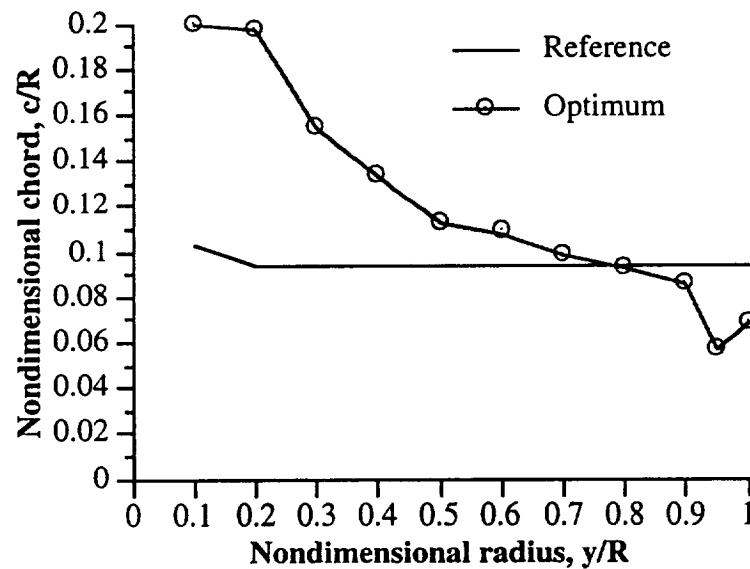


Figure 35  Chord distributions

The twist distributions ($\theta$) are presented in Fig. 37. The twist is reduced from reference to optimum values over the inboard section of the blade and is increased over the midspan section. At the outboard section of the blade, the twist remains almost unchanged after optimization. It must be noted from Fig. 37 that the largest differences between reference and optimum, in both inboard and midspan locations, are of the order of two degrees. However, the increase is achieved in a region of the blade which has greater resultant velocities. This reduces the collective pitch of the blade thereby reducing the overall angle of the attack of the blade. The result is a more even distribution of the angle of attack throughout the blade which subsequently reduces the drag

(Fig. 38a,b). The minimal changes in the angle of attack distribution in case of high speed cruise, between reference and optimum, partially explains the very small improvements obtained in $\eta_c$.
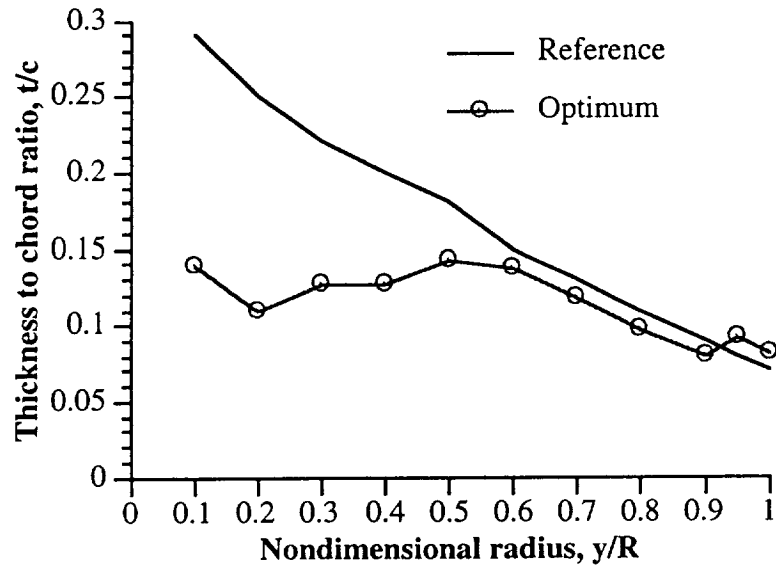


Figure 36  Thickness to chord ratio distributions
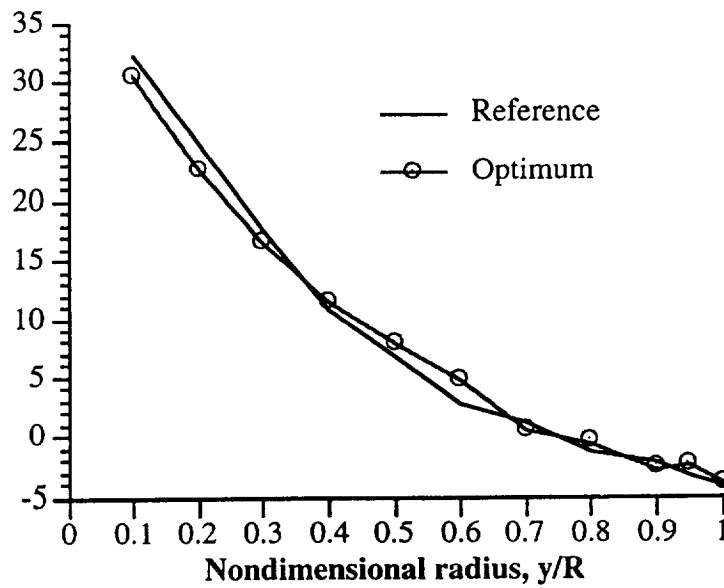


Figure 37  Blade twist distributions
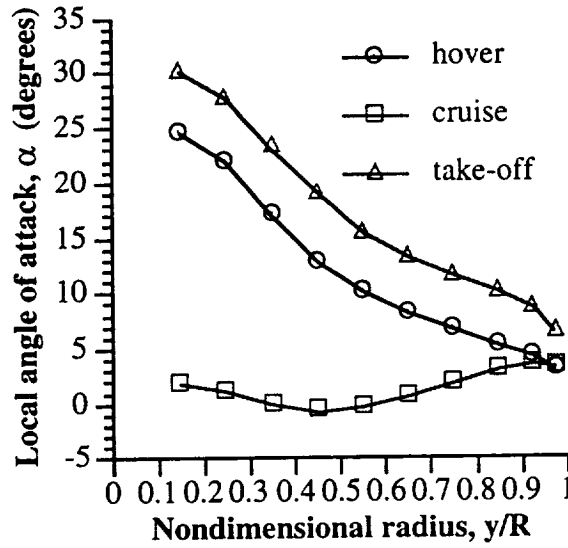
Figure 38a. Reference blade angle of attack   Figure 38b. Optimum blade angle of attack
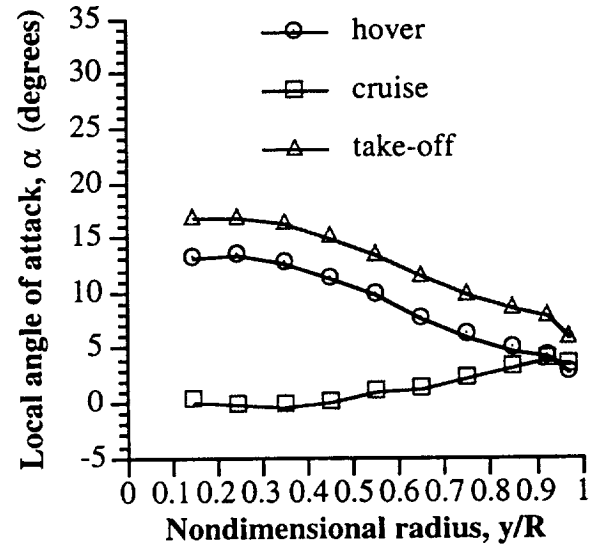
Figure 39 shows the zero lift angle of attack distributions ($\alpha_{zl}$) for both the reference and the optimum rotors. Significant decreases are observed from the reference values except at the tip. The result is an increase in airfoil camber which improves the lift-to-drag ratio thereby improving performance. However, associated with increased camber is higher drag divergence Mach numbers ($M_{dd}$) which can adversely affect the cruise performance. Therefore to avoid large drag penalties caused by operating the blade at local Mach numbers above $M_{dd}$, the zero lift angle of attack is only slightly reduced at the tip.

The rotor planform remains unswept after optimization. This is explained as follows. Since only static loading is included in this study and no aeroelastic stability requirements are imposed, the sweep of the blade was constrained during optimization such that the rotor could only be swept backwards. However, backward sweep induces large nose down pitching moments which increases the magnitude of the elastic twist which is used as an objective function and is minimized at each flight condition. As a result, the optimizer avoids sweeping the blades to remain in the feasible domain.
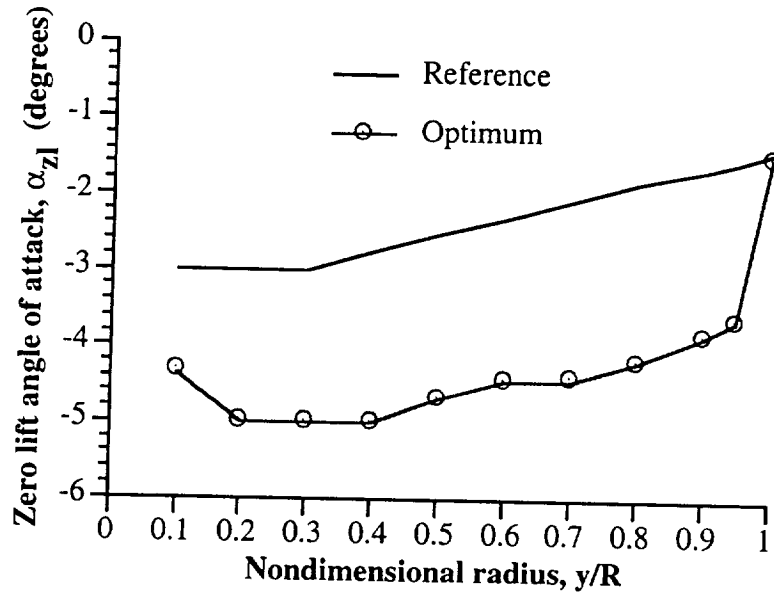
Figure 39  Zero lift angle of attack distributions
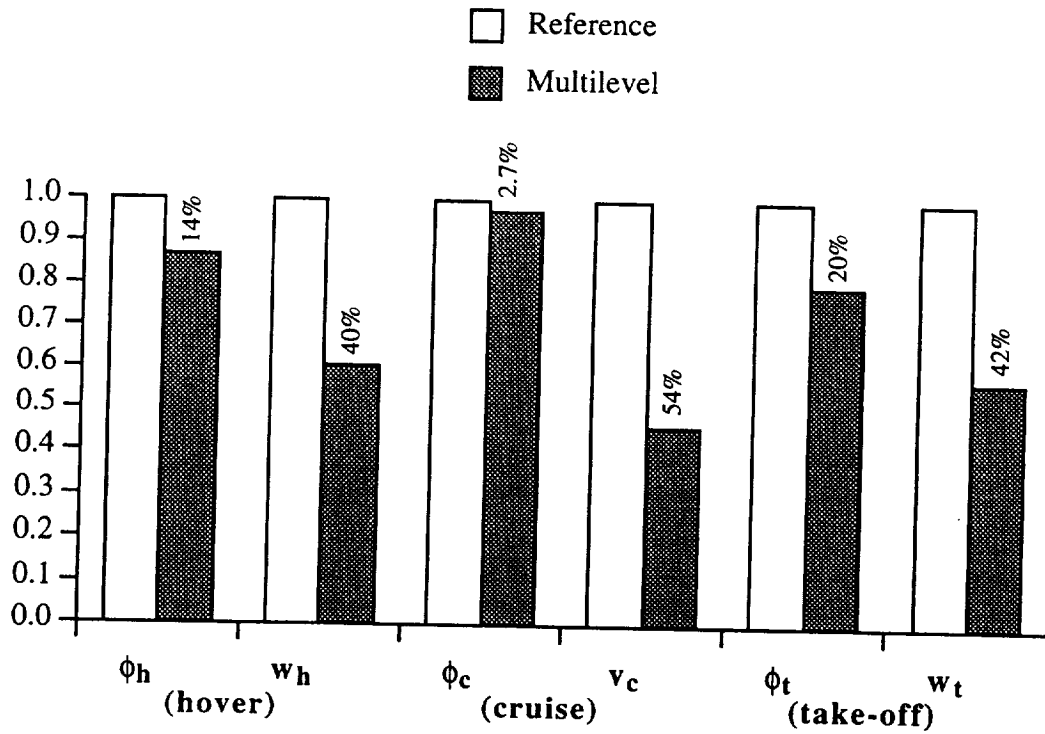


Figure 40  Summary of lower level objective functions

The lower level objective functions are presented in Table 5 and in Fig. 40 where large reductions from the reference rotor are observed in all six objective functions. The elastic twist in

hover ($\phi_h$), in cruise ($\phi_c$) and in take-off ($\phi_t$) are reduced by 14, 2.7 and 20 percent, respectively. The vertical displacement in hover ($w_h$) is reduced by 40 percent and in take-off ($w_t$) by 42 percent. The horizontal displacement in cruise ($v_c$) is reduced by 54 percent.

The composite laminate stacking sequences are presented in Table 6. Note that in the reference blade, the horizontal and vertical walls are assumed to have the same stacking sequence. Further, since all of the laminates are considered to be symmetric about their midplane, only 12 of the 24 total plies are presented in the table for each wall. The individual ply thickness used in this study is 0.001 in. which results in a total wall thickness of 0.24 in. The rearrangement of the stacking sequence after optimization represents a compromise between the conflicting requirements of reduced elastic twist and reduced transverse displacements. This is observed by noting the inclusion of ±30 degree plies in both the horizontal and the vertical walls.

Table 6 Ply orientation angles

| Reference | | Optimum | |
| --- | --- | --- | --- |
| | | Horizontal Wall | Vertical Wall |
| Outer ply | 0° | 15° | 15° |
| | 0° | -15° | -15° |
| | 0° | 0° | 15° |
| | 0° | 0° | -15° |
| | 15° | 45° | 30° |
| | -15° | -45° | -30° |
| | 15° | 45° | 30° |
| | -15° | -45° | -30° |
| | 45° | 0° | 0° |
| | -45° | 0° | 0° |
| | 45° | 30° | 15° |
| midplane | -45° | -30° | -15° |

The elastic twist ($\phi$) distributions of the reference and optimum rotors are presented in Fig. 41. The figure shows that the elastic twist distributions are reduced in magnitude after optimization throughout the blade span in all three flight conditions. Note that the elastic twist values are all negative resulting in a nose down motion. Similar trends are observed in case of the transverse vertical displacement, the transverse horizontal displacement and the axial displacement. The reductions in all of the displacement distributions are attributable to the improved ply stacking

57

sequence and the increased thickness of the airfoil due to larger chords which in turn increases the box beam height.
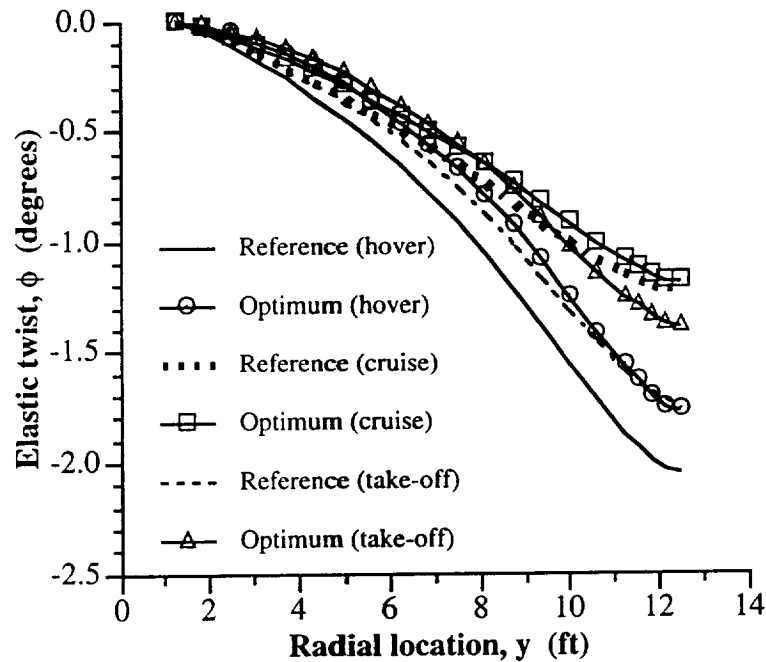


Figure 41  Elastic twist displacements

## 5.5  Concluding Remarks

A multiple design point optimization procedure was developed for the design of high speed prop-rotors. A multilevel decomposition optimization technique was used to decompose the problem into two levels. Aerodynamic performance was the objective of the upper level and the structural response was improved at the lower level. Optimization was performed simultaneously to include high speed cruise, hover and take-off. The Kreisselmeier-Steinhauser function was used to formulate the multiple objective optimization problems at each level. At the upper level, a nonlinear programming technique based on the Broyden-Fletcher-Goldfarb-Shanno method was used as the optimization algorithm. A simulated annealing algorithm was used for the discrete optimization problem at the lower level. A total of 5 global cycles were required for convergence. The optimum results were compared with a reference rotor. Following are some important observations.

1. The multilevel optimization procedure significantly improves the aerodynamic and structural response of the high speed prop-rotor blade at all three flight conditions.

2. The chord distribution of the optimum rotor closely resembles the ideal hover chord distribution. Exceptions are noted at the root and at the tip where the optimizer is driven by the geometric constraints imposed on the problem.

3. The airfoil thickness to chord ratio is significantly decreased at inboard section of the blade after optimization. This reduces the profile drag over this portion of the blade which improves the performance.

4. The optimum twist is reduced at inboard sections, increased over the mid section and remains largely unchanged at outboard sections. The result is a more optimum distribution of the local angle of attack which improves performance in hover and in take-off. The tip twist remains unchanged to maintain efficiency in high speed cruise.

5. The airfoil camber of the optimum blade is significantly increased from reference values to improve the airfoil lift-to-drag ratio resulting in increased aerodynamic efficiency.

6. The simulated annealing algorithm successfully minimizes the tip displacements by altering the composite plate stacking sequences in the horizontal and vertical walls. The optimum composite stacking sequence represents a compromise between reduced elastic twist and reduced transverse deformation. This is manifested through the selection of ±30 degree plies in both the horizontal and the vertical walls.

7. A combination of improved stacking sequence and larger chord values leads to reduced elastic deformation in the optimum configurations.

# 6. Coupled Rotor/Wing Optimization

Recently, research efforts have been initiated by Chattopadhyay et al. [4,5,15-18,29] to develop formal optimization techniques to address the conflicting issues involving tilt-rotor design. In Refs. 4 and 15 optimization procedures were developed to maximize the high speed cruise propulsive efficiency without degrading the hover figure of merit. The problem of individual blade aeroelastic stability in high speed cruise was included in the optimization formulation in Ref. 16. In Ref. 17, the drive system weight was minimized and the associated trade-off in cruise efficiency was investigated. The integrated aerodynamic, aeroelastic and structural optimization of the rotor was addressed in Ref. 5. In Ref. 18, a purely aerodynamic multiobjective optimization procedure was reported for improved high speed cruise and hovering performance using planform and airfoil characteristics as design variables. In Ref. 29, the aerodynamic and structural design criteria in both high speed cruise and hover were addressed by developing a multilevel decomposition based optimization procedure. In all of the above work, the rotor design was the primary concern and only the rotor planform parameters and geometric properties were included as design variables in the optimization formulation.

The influence of the wing, however, is a critical design issue and requires in-depth study. Therefore, the development of a multidisciplinary optimization procedure involving simultaneous rotor-wing design is important in helping to understand the various instabilities which ultimately affect the aircraft performance. This study represents the results of a recent research effort aimed at studying the various trade-offs associated with such a design. In this study, the designs of the rotor and the wing are simultaneously addressed using formal optimization techniques.

## 6.1 Rotor/Wing Geometric Modeling

The reference rotor is the representation of the XV-15 rotor which was used in the previous objectives. The rotor is a three-bladed, gimballed rotor. The wing representation is based on the same aircraft configuration in which the rotor are mounted at the wing tips. The dynamic behavior of the wing is characterized by the first six frequencies, generalized masses and mode shapes of the

the load carrying member. The reference quantities correspond to the NASTRAN data of the XV-15 tilting prop-rotor aircraft [9,10,30].

### 6.1.1 Rotor Model

The rotor planform characteristics are defined as follows. The chord, $c(\bar{y})$, twist angle of attack, $\theta(\bar{y})$ and the lifting line offset, $x_{ac}(\bar{y})$, are defined to have the following cubic spanwise distributions.

$$\theta(\bar{y}) = \theta_1(\bar{y} - 0.75) + \theta_2(4(\bar{y} - 0.75)^2 - 3(\bar{y} - 0.75))$$
$$+ \theta_3(15(\bar{y} - 0.75)^3 - 20(\bar{y} - 0.75)^2 + 6(\bar{y} - 0.75)) \tag{31}$$

$$c(\bar{y}) = c_0 + c_1\bar{y} + c_2(4\bar{y}^2 - 3\bar{y}) + c_3(15\bar{y}^3 - 20\bar{y}^2 + 6\bar{y}) \tag{32}$$

where $\theta_1$-$\theta_3$ and $c_0$-$c_3$ represent coefficients describing the spanwise variations of twist and chord, respectively. The offset in the twist distribution ($\bar{y}$-0.75) is used to ensure zero twist at 75 percent span. The shape functions used in these distributions are selected to maintain orthogonality between the functions over the range 0 to 1 which is beneficial to the optimization algorithm.

A perturbational model, based on the chord distribution, is used to calculate the structural properties. The blade stiffness properties are assumed to vary from the reference values, which is the same baseline configurations as in the previous objectives, as follows.

$$\frac{EI_{xx}}{EI_{xx_{ref}}} = \left(\frac{c(\bar{y})}{c_{ref}(\bar{y})}\right)^4 \tag{33}$$

where $EI_{xx}$ is the flapping stiffness and $c(\bar{y})$ is the chord. The lagging stiffness ($EI_{zz}$), the torsional rigidity (GJ) and the polar moment of inertia ($I_\theta$) are defined similarly. The fourth order relation is used since, in general, these quantities are based on fourth order dependence of the beam width and height. Assuming that these quantities are directly proportional to the chord, the fourth order dependence on the chord is obtained. The blade sectional mass and radius of gyration distributions, $m(\bar{y})$ and $k_r(\bar{y})$, respectively, are assumed to be quadratic as follows.

61

$$\frac{m}{m_{ref}} = \left(\frac{c(\overline{y})}{c_{ref}(\overline{y})}\right)^2 \quad \text{and} \quad \frac{k_r}{k_{r_{ref}}} = \left(\frac{c(\overline{y})}{c_{ref}(\overline{y})}\right)^2 \tag{34}$$

The quadratic dependence is assumed for these quantities since they tend to be dependent on the cross-sectional area, which again is assumed to directly proportional to the chord. Similarly, the center of gravity, tension center and lifting line offsets from the elastic axis are assumed to vary linearly with the chord ratio.

### 6.1.2 Wing Model

The aircraft wing is modeled as a cantilevered beam with tip masses representing the rotor system, transmission and engine pylon (Fig. 42). Although the reference wing planform is rectangular, the wing chord (C) is assumed to be linearly tapered to allow additional freedom to the optimizer as follows.

$$C = C_r \left[1 + \varsigma(\lambda - 1)\right] \tag{35}$$

where $C_r$ is the root chord, $\varsigma$ is the nondimensional wing span, $\lambda$ is taper ratio ($\lambda = C_t/C_r$ where $C_t$ is the tip chord).

The load carrying structural member in the wing is modeled as a rectangular isotropic box beam with four independent wall thicknesses (Fig. 43). To reduce the number of design variables while keeping the design space sufficiently large, spanwise variations of wall thicknesses are assumed to be similar to the rotor chord and twist distributions as follows.

$$t_i(\varsigma) = t_{i_0} + t_{i_1}\varsigma + t_{i_2}(4\varsigma^2 - 3\varsigma) + t_{i_3}(15\varsigma^3 - 20\varsigma^2 + 6\varsigma) \tag{36}$$

where the coefficients $t_{i_0}$ - $t_{i_3}$ describe the thickness distribution in each of the four walls (i=1, 2, $\cdots$ , 4).

### 6.2 Optimization Problem

The coupled rotor/wing optimization problem is performed simultaneously under three different flight conditions. The first flight condition corresponds to sea level hover and the second flight

condition represents high speed cruise at an altitude of 25,000 feet. The third condition, which is used to investigate the aeroelastic stability of the coupled system, is a high speed windmill condition performed at an altitude of 25,000 feet.
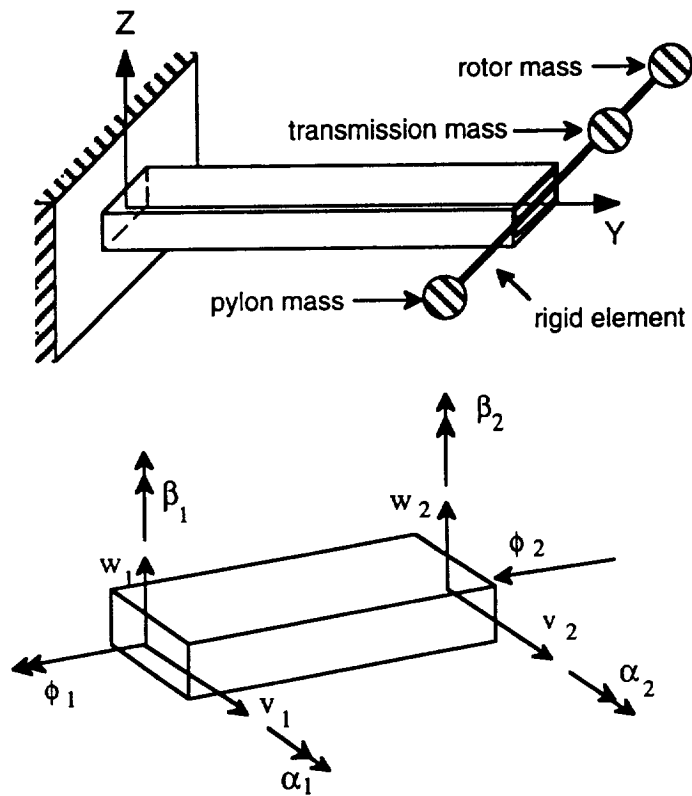

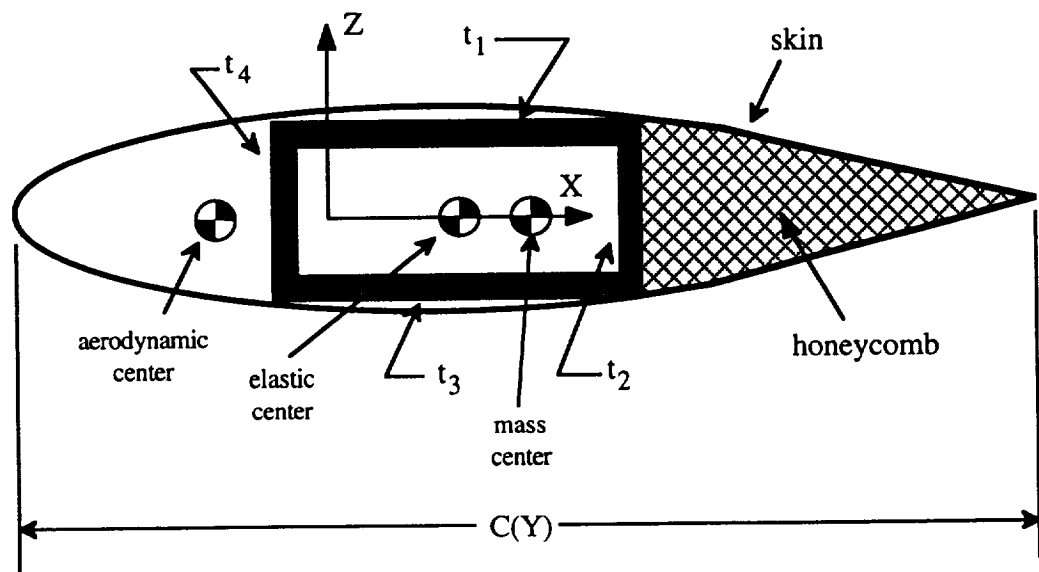
Figure 42  Aircraft wing modeling



Figure 43  Wing cross section

### 6.2.1 Objective Functions

The optimization problem addresses the multiple design requirements of maximizing the hover figure of merit (FM) and the propulsive efficiency in high speed cruise ($\eta_c$) as well as minimizing the wing weight ($W_{wing}$) simultaneously. The wing weight is defined as follows.

$$W_{wing} = (1 + \varepsilon) \int_0^b \rho A dx \qquad (37)$$

where A is the cross-sectional area of the box beam, $\rho$ is the density of the beam and b is the wing span. The factor $\varepsilon$ is used to include the effect of the nonstructural weight which is assumed to be one third of the structural weight.

### 6.2.2 Constraints

The following constraints are included in the optimization procedure to ensure efficient rotor and wing performance. To maintain rotor thrust at acceptable values during optimization, equality constraints are imposed on the thrust in hover and cruise. These constraints assume the following form.

$$T_h = T_{href} \text{ and } T_c = T_{cref} \qquad (38)$$

Additional constraints are imposed on the first natural frequency in hover ($f_1$), the autorotational inertia (AI) and the blade weight ($W_{blade}$). To avoid ground resonance, the first natural frequency is constrained to be a prescribed amount above 1/rev. The autorotational inertia is constrained to be no less than 90 percent of the reference value to ensure that the optimum rotor can sufficiently autorotate in the event of engine failure. Since the autorotational inertia of the reference rotor is large, the minimum value of 90 percent of the reference value is selected to allow the optimizer more flexibility during the optimization process. An upper bound is imposed on the blade weight so that any reductions in the wing weight, which is an objective function, are not offset by an increase in the blade weight. These constraints are stated as follows.

$$f_1 \geq (1 + \Delta)/\text{rev} \qquad (39)$$

64

$$AI \geq 0.9\, AI_{ref} \qquad (40)$$

$$W_{blade} \leq W_{ref} \qquad (41)$$

where $\Delta = 0.2$ represents a margin of safety which ensures that the first natural frequency in hover is above 1/rev.

Since both the rotor and the wing designs are altered during optimization, it is important to impose aeroelastic stability constraints to prevent any destabilization of the rotor/wing in high speed cruise. Since the rotor is wing tip mounted for tilting prop-rotors, the first several modes of airframe, which are important for whirl flutter, are dominated by wing motion. To impose a factor of safety into the stability, the whirl flutter calculations are performed at the maximum dive speed which is 20 percent above the cruise condition. Also, the blade is trimmed to the windmill condition. These constraints are expressed as follows.

$$\Lambda_k \leq -\upsilon \quad k = 1, 2, \cdots, NMODE \qquad (42)$$

where NMODE is the total number of modes considered in cruise and $\Lambda_k$ is the real part of the stability root. The quantity $\upsilon$ denotes the minimum allowable blade damping and is defined to be equal to 0.01.

Finally, constraints are imposed on the stresses at the root section of the wing box beam to ensure that the maximum stresses are below the allowable limit when multiplied by a factor of safety. These constraints assume the following form.

$$\tau_{oct} \times FS \leq \sigma_{al} \qquad (43)$$

where NSEG is the number of wing segments, $\tau_{oct}$ is the octahedral stress at the wing root, FS is the factor of safety and $\sigma_{al}$ is the allowable stress. These stresses are calculated in both hover and cruise although they are more critical in hover.

### 6.2.3 Design Variables

To study the trade-offs associated with the simultaneous design of the rotor and the wing, design variables pertaining to both the rotor and the wing are used during optimization. The design

variables for the rotor include the coefficients which define the spanwise chord and twist distributions ($c_0$ - $c_3$ and $\theta_1$ - $\theta_3$, respectively). As mentioned before, the shape functions used to describe the twist and the chord distributions are chosen to ensure orthogonality of the functions. Similarly the parameters that define the individual wall thicknesses in the wing-box ($t_{ij}$) are used as design variables. The wing root chord ($C_r$) and taper ratio ($\lambda$) are also included as design variables. It must be noted that in order to ensure that the blade chord and wing thickness distributions are realistic (that is, positive throughout the span) it is necessary to further impose geometric constraints on these distributions.

## 6.3 Analysis

This section briefly describes the analysis procedures which are coupled within the optimization loop. This is followed by a description of the optimization technique.

### 6.3.1 Rotor Analysis

The analyses is performed using a comprehensive rotary wing analysis technique as implemented in the code CAMRAD [31]. The program calculates the section loading from the airfoil two-dimensional aerodynamic characteristics. It uses the lifting line or blade element approach and has corrections for yawed and three-dimensional flow effects. A wind tunnel trim option is used and the rotor is trimmed to a specific $C_T/\sigma$ value ($C_T$ is the coefficient of thrust and $\sigma$ is the area-weighted solidity of the rotor) using the collective blade pitch. The value of $C_T/\sigma$ is calculated based on the prescribed values of thrust required at each flight condition. For the flutter calculations, a wind tunnel trim analysis is also performed. However, since this case is meant to be representative of a windmilling rotor, the rotor is trimmed to zero power. The aeroelastic stability analysis is performed using an assumption of axisymmetric flow. The blade is discretized into 51 structural elements and 24 aerodynamic elements. Six bending degrees of freedom, six torsional degrees of freedom and two gimbal degrees of freedom are used to model the rotor. The first six symmetric wing modes are also included in the whirl flutter calculations to yield a total of 40 flutter modes. To reduce the computational effort, uniform inflow is assumed in all cases. The

blade response is calculated in CAMRAD using rotating free-vibration modes equivalent to a Galerkin analysis. The blade is trimmed at each optimization cycle so that an intermediate design, which is a feasible design, represents a trimmed configuration.

### 6.3.2 Wing Analysis

The wing aerodynamic and dynamic analysis is performed using an in-house developed code based on finite element analysis. The natural frequencies, generalized masses and generalized mode shapes of the wing are then used as inputs to describe the airframe, as required by CAMRAD. The load carrying member of the wing is modeled as a box beam with a rectangular cross section (Fig. 43). Ten degrees of freedom are used to represent each beam element (Fig. 42). To model the geometric offset between the rotor hub and the elastic axis of the wing box beam, rigid elements are included at the wing tip. The cross-sectional properties of every beam element are calculated using thin wall theory. To obtain a realistic wing representation, the reference configuration used in the optimization procedure is based on an untapered chord and wall thickness distributions.

The aerodynamic effects on the wing are evaluated using the lifting line theory with the assumption of quasi-steady aerodynamics which is used to compute the local lift coefficient distribution along the wing span. The aerodynamic forces are divided into a conservative part, which is analogous to a mechanical spring and a non conservative part which represents an aerodynamic damper.

The derivation of the aerodynamic forces on a typical wing element is described here. Referring to Fig. 43 and assuming that the lift (L) acts at the quarter chord at a distance $X_a$ from elastic center, the lift can be expressed as follows.

$$L = -\frac{1}{2}\rho_\infty V_\infty^2 C c_{l\alpha}\left[\alpha_w + \frac{\dot{w}}{V_\infty}\right] \tag{44}$$

where $\rho_\infty$ is the air density, $V_\infty$ is the flight speed, C is wing chord length, $c_{l\alpha}$ is the lift curve slope, $\alpha_w$ is the wing angle of attack and $\dot{w}$ is the velocity in the Z direction (Fig. 43). The work done by the aerodynamic force is then defined as follows.

$$W = \frac{1}{2}\int_0^{l_e} \dot{L}(w - \alpha_w X_a)dX \qquad (45)$$

where $l_e$ is the element length and w is the vertical displacement. Denoting

$$\Gamma = \frac{1}{2}\rho_\infty V_\infty^2 C c_{l\alpha} \qquad (46)$$

and substituting into Eqn. 45 yields the following.

$$W = -\frac{1}{2}\int_0^{l_e} \Gamma\alpha_w(w - X_a\alpha_w)dX - \frac{1}{2}\int_0^{l_e} \frac{\Gamma}{V_\infty}\dot{w}(w - X_a\alpha_w)dX \qquad (47)$$

The first integral in Eqn. 47 represents the conservative work, $W_1$ and the second integral, $W_2$, represents the non conservative work. Using a finite element approximation these quantities can be expressed as follows.

$$W_1 = -\frac{1}{2}x^T K_w x, \quad W_2 = -\frac{1}{2}\dot{x}^T C_w x \qquad (48)$$

where x is the nodal displacement vector, $K_w$ and $C_w$ are analogous to the stiffness and damping matrices, respectively, normally associated with structural formulations and $\dot{x}$ is the time derivative of the nodal displacements.

## 6.4 Optimization

In this study, multiple objective functions are chosen and therefore the Kreisselmeier-Steinhauser (K-S) function is used to formulation the multiobjective optimization problem. Since the objective functions and the constraints must be evaluated several times before convergence is achieved, calculation of these values using exact analyses at each iteration is computationally prohibitive. Therefore the objective functions and constraints are approximated using a two-point exponential hybrid approximation technique. Details of these techniques are found in Chapters 3-5.

## 6.5 Results

The same reference rotor is again used for this study. The aerodynamic optimization is performed at a cruise altitude of 25,000 feet and a forward velocity of 300 knots with a rotational speed of 421 RPM. A vehicle weight of 13,000 pounds and, in this objective, an aircraft lift-to-drag ratio (L/D) of 5.3 are assumed. Therefore, the thrust in cruise is constrained to be 1226 pounds for the two engine aircraft. In hover, the aircraft is assumed to be operating at sea level conditions with a rotational speed of 570 RPM. A 12 percent download effect from the rotor/wing interaction is used so that the thrust in hover is constrained to be 7280 pounds. The flutter calculations are performed at a speed 20 percent above the cruise speed to represent the maximum dive speed (360 knots) and an altitude of 25,000 feet with a rotational velocity of 421 RPM. The blade is trimmed to the windmill condition for the calculation of the flutter roots. The operating conditions are summarized in Table 7.

### Table 7  Summary of flight conditions

| | |
|---|---|
| Vehicle weight | 13,000 lb |
| Blade radius | 12.5 |
| **Hover** | |
| Altitude | Sea level |
| Thrust, $T_h$ | 7280 lb |
| Rotational speed | 570 RPM |
| **Cruise** | |
| Altitude | 25,000 ft |
| Thrust, $T_c$ | 1226 lb |
| Rotational speed | 421 RPM |
| Forward speed, $V_\infty$ | 300 knots |
| **Flutter** | |
| Altitude | 25,000 ft |
| Power, $C_p$ | 0.0 |
| Rotational speed | 421 RPM |
| Forward speed, $V_\infty$ | 360 knots |

The results from the optimization are presented in Table 8 and Figs. 44 - 55. From Table 8 and Fig. 44, it is seen that the aerodynamic objective functions are both improved. The hover figure of merit is increased by 2.3 percent while the propulsive efficiency in high speed cruise is slightly increased (0.3 percent) after optimization. A comparison of the weights is presented in Table 8 and

69

Fig. 45 where it is seen that the wing weight ($W_{wing}$), which is also an objective function, is reduced by 14 percent from the reference value. The blade weight ($W_{blade}$) which is included only as a constraint is also reduced significantly (6.3 percent) from the reference value. Further, the total rotor/wing weight which is defined for the three bladed rotor as

$$W_{total} = W_{wing} + 3\,W_{blade} \tag{49}$$

is reduced by over 10 percent. These trends can be explained by examining the rotor and wing planforms.

Table 8  Summary of optimum results

| | Bounds | | Reference | Optimum |
|---|---|---|---|---|
| | Lower | Upper | | |
| *Objective functions* | | | | |
| FM | | | 0.7246 | 0.7411 |
| $\eta_c$ | | | 0.8475 | 0.8502 |
| $W_{wing}$ | | | 704.3 | 606.1 |
| *Constraints* | | | | |
| $f_1$ (per rev) | 1.200 | - | 1.291 | 1.327 |
| AI (lb-ft$^2$) | 3430 | - | 3811 | 3465 |
| $W_{blade}$ (lb) | - | 213.4 | 213.4 | 200.0 |
| | | | | |
| $W_{total}$ (lb) | - | - | 1345 | 1206 |

The rotor blade chord distributions are presented in Fig. 46 and show that after optimization the blade chord has reduced values near the root and at the tip. This is due to the conflicting requirements posed by the hover and the cruise flight conditions. In hover, the rotor blade encounters negative angles of attack ($\alpha_b$) at the tip which degrades performance (Fig. 47). The optimizer cannot simply reduce the twist at this location as this will degrade the high speed cruise propulsive efficiency. Similarly, the angle of attack distribution of the blade is negative near the root for the cruise condition (Fig. 48) and a simple increase in the twist at this location, to alleviate this problem, would degrade the hover figure of merit. The optimizer finds a compromise by

slightly reducing the twist near the root (Fig. 49) which favorably alters the collective trim angle, but more importantly by increasing the chord over the midspan region of the blade which is beneficial to both flight conditions. The chord is then reduced near the root to improve the high speed cruise propulsive efficiency and is reduced at the tip to improve the hover figure of merit.
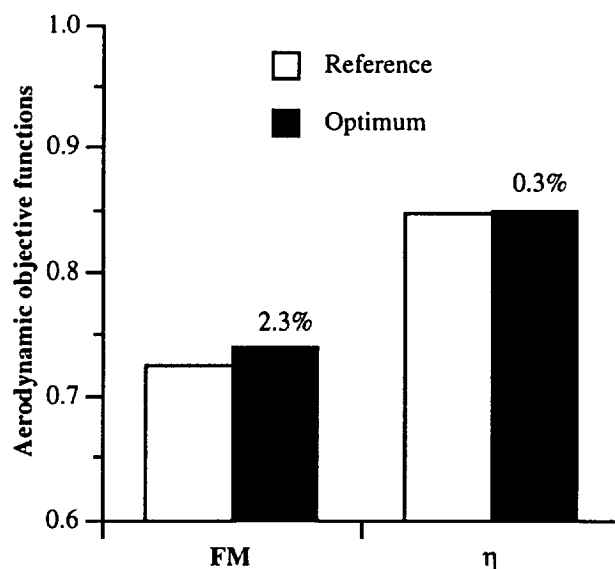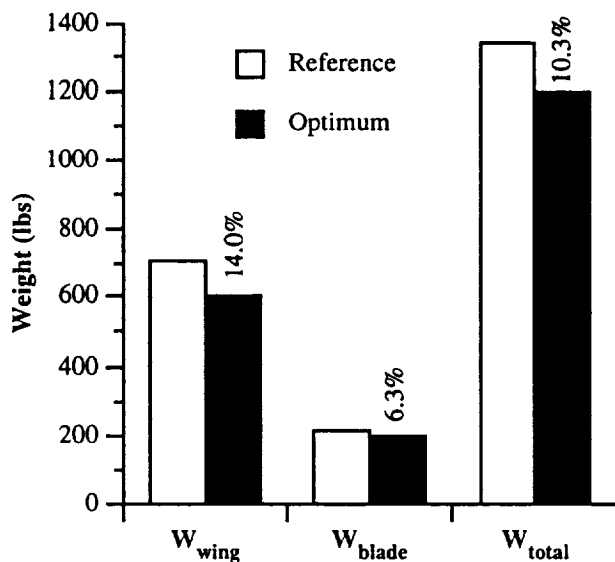
Figure 44  Optimum aerodynamic results

Figure 45  Optimum structural results

71
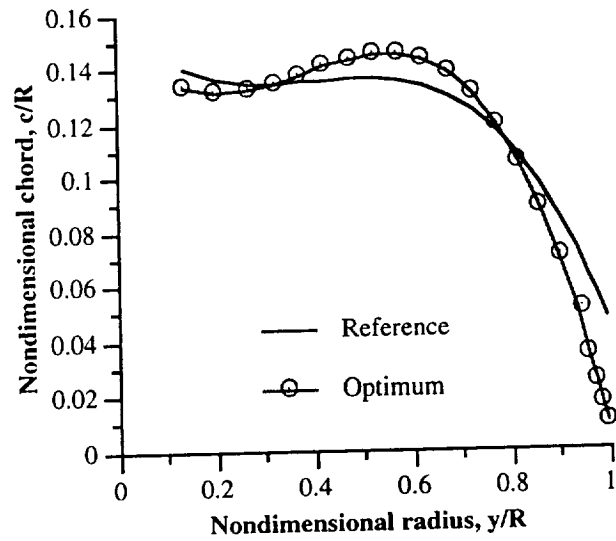
Figure 46  Blade chord distributions
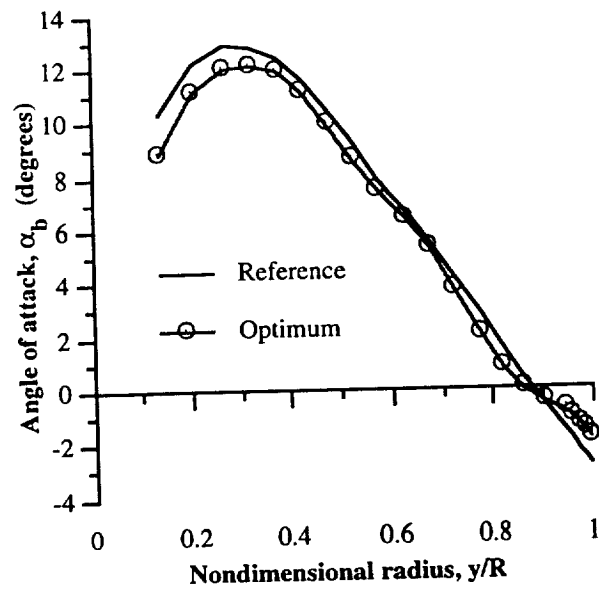


Figure 47  Hover angle of attack distribution

72
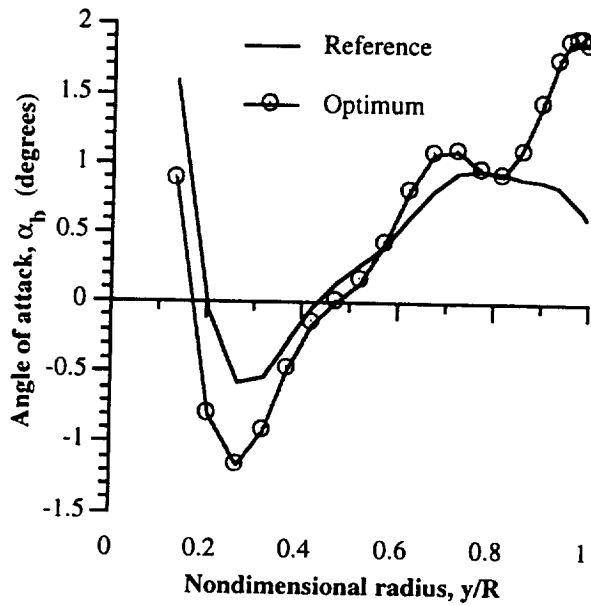
Figure 48  High speed cruise angle of attack distribution
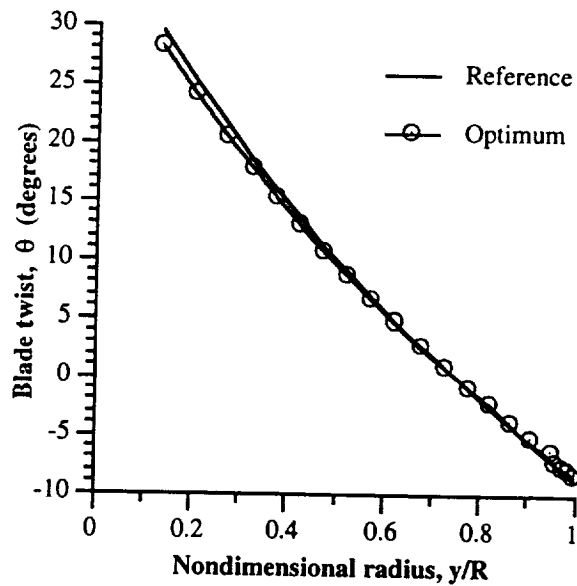


Figure 49  Blade twist distributions

The wing chord distributions are presented in Fig. 50. It is seen from this figure that the root chord remains unchanged and a very small amount of taper is introduced ($\lambda = 0.99$). Since the critical stresses occur at the root, the optimizer allows slight taper in the wing chord distribution which in turn tapers the dimensions of the box beam without exceeding the allowable stresses. If too much taper is introduced to reduce the weight, the stiffness of the beam will be reduced and the

aeroelastic stability will be degraded. This is why only a small taper is permissible in the wing chord distribution.



Figure 50  Wing chord distributions

The horizontal wall thickness of the wing box beam are presented in Fig. 51a. From the figure it is interesting to note that although the reference distributions for the top and the bottom walls are initially different, after optimization they are almost identical. The trend is to increase the thicknesses at the percent span. Near the tip, the thicknesses are slightly above the value at 75 percent span location but are still drastically reduced from the reference values (28.5 and 22.5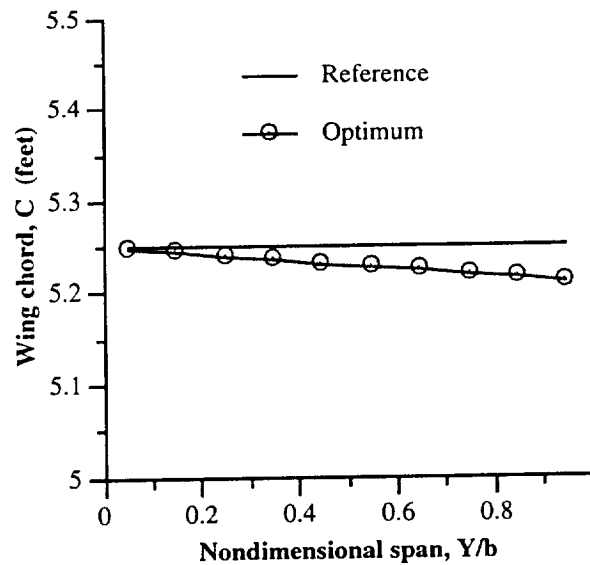 percent, respectively for the top and bottom walls). This is explained as follows. Near the root, the thicknesses are increased to satisfy the stress constraints which are initially violated. Since only the root stresses are included as constraints, the optimizer is now able to reduce the distributions throughout the span in order to reduce the wing weight. To ensure that the aeroelastic stability constraints are not violated (Fig. 52), the thicknesses near the tip are held nearly constant (relative to the 75 percent span value). The very small increases in the tip values, from the 75 percent span location, are due to the nature of the orthogonal functions used in the formulation of the thickness distributions. If more higher order orthogonal functions were included in the formulation, the tip values would very likely equal the values at 75 percent span. It must be noted

that the cause of the initial constraint violation of the reference wing is due to the assumption of the box beam model. In order to closely match the natural frequencies, generalized masses and generalized mode shapes of the actual structural assembly which consists of stringers, spars and webs, the thickness distribution of the rectangular box beam produces stress constraints which are slightly violated initially. The authors acknowledge that a more accurate representation of the wing structural elements is necessary for further studies.
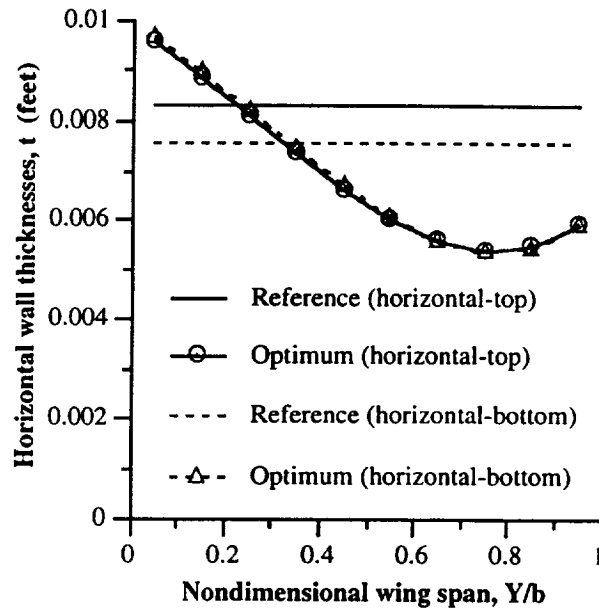


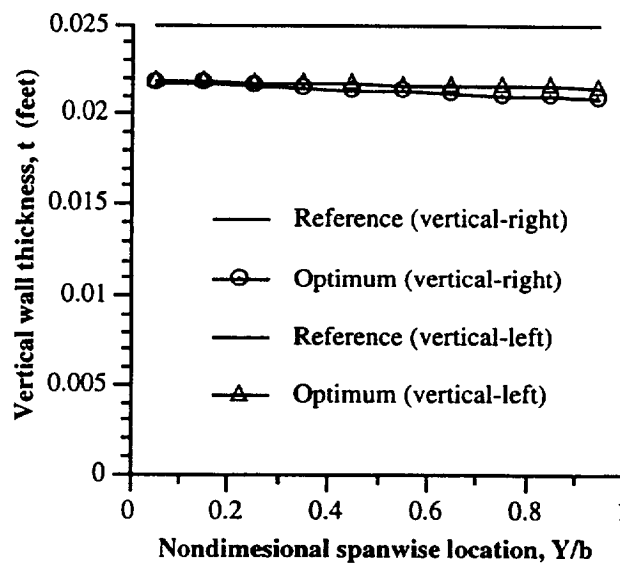Figure 51a  Horizontal wall thicknesses distributions



Figure 51b  Vertical wall thicknesses distributions

The vertical wall thickness distributions are presented in Fig. 51b and shows that the optimum distributions are reduced from reference values throughout the blade span, including at the root. It must be noted here that the reference distributions in this case are the same for both the right and the left walls. The increased stiffnesses required to satisfy the stress constraints were achieved through an increase in the root thickness of the horizontal walls. Therefore, the optimizer is able to reduce the vertical wall thicknesses throughout the blade span to reduce the wing weight. It is of interest to note that despite the fact that cubic distributions are assumed for the vertical wall thicknesses, the optimum distributions in both cases essentially have only slight linear taper.
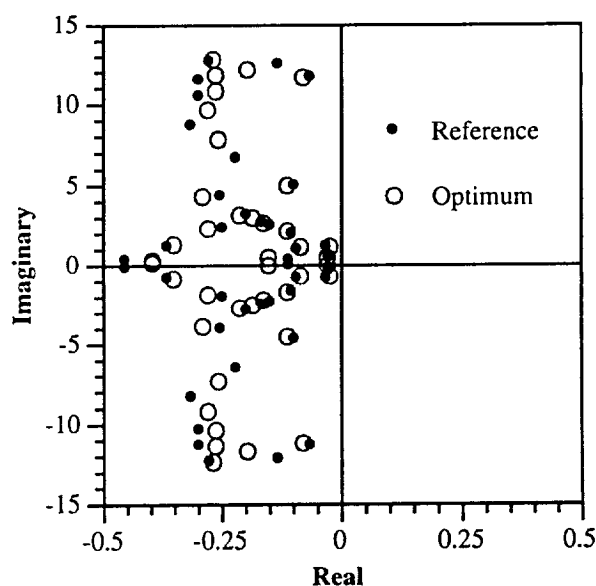


Figure 52  Aeroelastic stability characteristic exponents

The first three mode shapes for the wing are presented in Figs. 53 - 55. The first mode (Fig. 53) is primarily an out-of-plane (flapping) motion. The second mode (Fig. 54) represents a primarily in-plane (chordwise bending) motion and the third mode (Fig. 55) is a elastic twist dominated motion. The figures also show the primary coupling associated with each mode. In Fig. 53 it is seen that the flapping motion of the first mode is slightly reduced from reference to optimum configuration. The coupling due to the pitching motion, however, is actually slightly increased in this mode. From Fig. 54 it is seen that the modes shapes for the second mode, which is primarily a lagging mode, are virtually unchanged after optimization. The third mode, which

represents a pitching dominated mode, is presented in Fig. 55 where it is again seen that primary mode is slightly reduced from reference to optimum, but the coupling, which in this case is due to the flapping motion, is again increased. The slight increases in the coupling of the wing modes are explained as follows. Wing weight minimization, one of the objectives, is accomplished through reductions of the wall thicknesses in the wing box beam and through the introduction of a slight wing chord taper. This results in small decreases in the wing stiffnesses and therefore small increases in the coupling of the mode shapes. A significant reduction in stiffnesses can increase whirl flutter instabilities. However, as shown in Fig. 52, although the aeroelastic stability constraints are made slightly more critical after optimization, they still remain stable. This is an important phenomenon and points to the critical trade-offs associated with optimum design for minimum wing weight while maintaining aeroelastic stability.
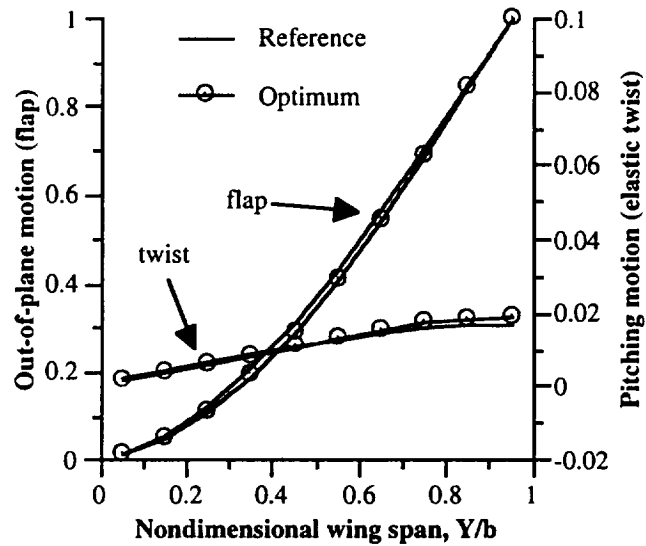


Figure 53 First wing mode
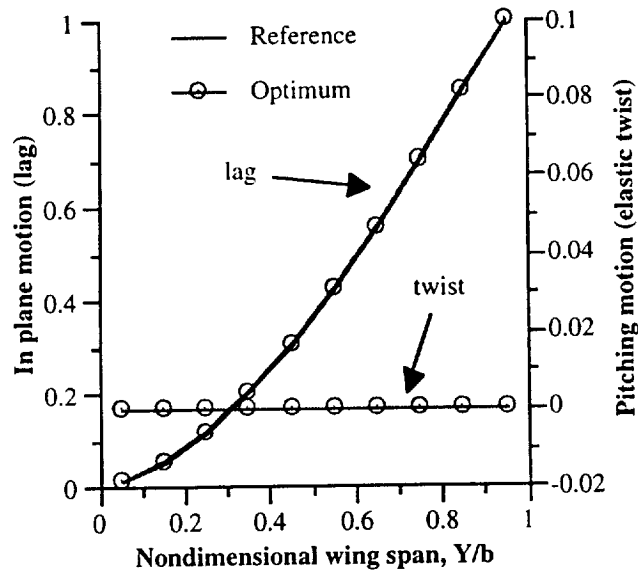
Figure 54  Second wing mode
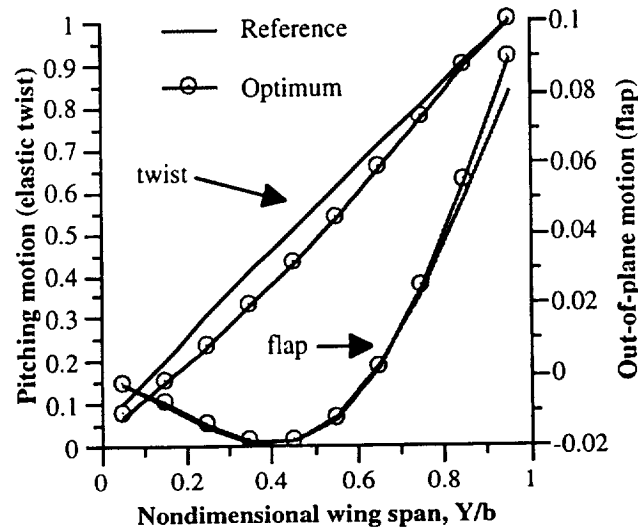


Figure 55  Third wing mode

## 6.6  Concluding Remarks

A multidisciplinary optimization procedure is developed to analyze the coupled rotor/wing design for prop-rotor aircraft. The optimization procedure couples aerodynamic performance, aeroelastic stability and structural design for both high speed cruise and hover flight conditions. Objective functions include the maximization of the hover figure of merit and the high speed cruise propulsive efficiency and minimization of the wing weight. Constraints are imposed on the first

natural frequency in hover, the autorotational inertia, the blade weight and the maximum wing root stresses  To prevent whirl flutter, constraints are also imposed on the real part of the stability roots. In addition, geometric constraints are also imposed.  The optimization procedure is performed using the Kreisselmeier-Steinhauser (K-S) function technique and the Broyden-Fletcher-Goldfarb-Shanno (BFGS) algorithm.  To reduce computational effort, an approximate analysis procedure based on the two-point exponential expansion and variable move limits is used.  The results obtained are compared with an existing reference tilt-rotor configuration.  The following important observations are made from this study.

1. Significant improvements are obtained in hover figure of merit and wing weight with small improvements in high speed cruise propulsive efficiency.  The combined rotor/wing weight is also reduced significantly.

2. The blade chord distribution is increased over the midspan region to exploit portions of the blade which simultaneously improve both the hover and high speed cruise performance. The chord distribution near the root and the tip are reduced due to the conflicting requirements posed by hover and cruise conditions.

3. Wing weight reductions are achieved through reductions in the wall thicknesses although the horizontal walls are increased at the root to satisfy the root stress constraints which are violated in the reference design.  The wing chord is only slightly tapered to maintain aeroelastic stability requirements.

4. Reduction in wing weight results in small reductions in stiffness in the optimum configuration.  This leads to increased coupling in wing modes.  However, stability is still maintained in the optimum configuration.

# 7. References

1. Dadone, L., Lui, J., Wilkerson, J. and Acree, C. W., "Proprotor Design Issues for High Speed Tiltrotors," Proc. 50th Annual Forum of the American Helicopter Society, Washington, DC, May 1994.

2. Felker, F. F., "Wing Download Results from a Test of a 0.658-Scale V-22 Rotor and Wing," Journal of the American Helicopter Society, Vol. 37, No. 4, October 1992, pp. 58-63.

3. Kreisselmeier, A. and Steinhauser, R., "Systematic Control Design by Optimizing a Vector Performance Index," *Proc.* of IFAC Symposium on Computer Aided Design of Control Systems, Zurich, Switzerland, 1979, pp. 113-117.

4. McCarthy, T. R. and Chattopadhyay, A, "Design of High Speed Proprotors Using Multiobjective Optimization Techniques," Paper No. AIAA 93-1032, *Proc. AIAA/AHS/ASEE Aerospace Design Conference*, Irvine, California, February 16-19, 1993. Also, *Journal of Aircraft* (in press).

5. Chattopadhyay, A., McCarthy, T. R. and Madden, J. F., "An Optimization Procedure for the Design of Prop Rotors in High Speed Cruise Including the Coupling of Performance, Aeroelastic Stability and Structures" *Mathematical and Computer Modelling*, Special Issue on Rotorcraft, Vol. 19, No 3/4, pp.75-99, 1994. Also presented at the *49th Annual Forum of the American Helicopter Society*, St. Louis, Missouri, June 1993.

6. Smith, R. L., "Closed Form Equations for the Lift, Drag, and Pitching-Moment Coefficients of Airfoil Sections in Subsonic Flow," NASA TM 78492

7. Talbot, P. D., "Propeller Performance Program Using Blade Element Momentum Theory," Draft Working Paper, NASA Ames Research Center, September 1989.

8. Glauert, H., The Elements of Airfoil and Airscrew Theory, Cambridge University Press, Second Edition, 1948.

9. Felker, F. F., Young, L. A. and Signor, D. B., "Performance and Loads Data from a Hover Test of a Full-Scale Advanced Technology XV-15 Rotor," NASA TM-86854, January 1986.

10. Arrington, W. L., Kumpel, M., Marr, R. L., and McEntire, K. G.., "XV-15 Tilt Rotor Research Aircraft Flight Test Data Report," NASA CR 177406, June 1985.

11. Corrigan, J. and Schillings, J., "Empirical Model for Stall Delay Due to Rotation," *Proc. of the AHS Aeromechanics Specialists Conference*, San Francisco, January 19-21, 1994.

12. Vanderplaats, G. N., "CONMIN - A FORTRAN Program for Constrained Function Minimization," User's Manual, NASA TMX-62282, July 1987.

13. Fadel, G. M., Riley, M. F. and Barthelemy, J. M., "Two Point Exponential Approximation method for Structural Optimization," *Structural Optimization*, Vol. 2., pp. 117-224.

14. Kirkpatrick, S., Gelatt, C. D. Jr., Vecchi, M. P., "Optimization by Simulated Annealing", *Science* vol. 220, No. 4598, May 1983, pp. 671- 680.

15. Chattopadhyay, A. and Narayan, J., "Optimum Design of High Speed Prop-Rotors Using a Multidisciplinary Approach," *presented at the 48th Annual Forum of the American Helicopter Society*, Washington DC, June 1992, pp. 1167-1177.

16. Chattopadhyay, A., McCarthy, T. R. and Madden, J. F., "Structural Optimization of High Speed Prop Rotors Including Aeroelastic Stability Constraints," *Mathematical and Computer Modelling*, Special Issue on Rotorcraft, Vol. 18, No. 3/4, 1993, pp. 101-113,.

17. Chattopadhyay, A., McCarthy, T. R. and Madden, J. F., "A Design Optimization Procedure for Minimizing Drive System Weight of High Speed Prop-Rotors" *Engineering Optimization*, Vol. 23, No. 4, 1995, pp. 239-254.

18. McCarthy, T. R., Chattopadhyay, A., Talbot, P. D., and Madden, J.F., "A Performance Based Optimization of High Speed Prop-Rotors," *Journal of the AHS* (in press). Also Proc. of the American Helicopter Society Aeromechanics Specialists Conference, San Francisco, Jan. 1994.

19. Smith, E. C. and Chopra, I., "Formulation and Evaluation of an Analytical Model For Composite Box-Beams," *Journal of the American Helicopter Society*, Vol. 36, No. 3, July 1991, pp. 23-35.

20. Walsh, J. L., Young, K. C, Pritchard, J. I., Adelman, H. M.. and Mantay, W., "Multilevel Decomposition Approach to Integrated Aerodynamic/Dynamic/Structural Optimization of Helicopter Rotor Blades," Proc. of the American Helicopter Society Aeromechanics Specialists Conference, San Francisco, Jan. 1994.

21. Chattopadhyay, A., McCarthy, T. R and Pagaldipti, N., "A Multilevel Decomposition Procedure for Efficient Design Optimization of Helicopter Rotor Blades," Proc. 19th European Rotorcraft Forum, Cernobbio, Italy, Paper n° G7, Sep. 1993.

22. Tsai, S. W. and Wu, E. M., "A General Theory of Strength for Anisotropic Materials," *Journal of Composite Materials*, 5, pp. 58-80, 1971.

23. Haftka, R. T., Gürdal, Z. and Kamat, M. P., Elements of Structural Optimization, Kluwer Academic Publishers, Dordrecht, The Netherlands, 1990.

24. Olsen, G. R. and Vanderplaats, G. N., "Method for Nonlinear Optimization with Discrete Design Variables", *AIAA Journal*, Vol. 27, No. 1, Nov. 1989, pp. 1584-1589.

25. Lombardi, M., Haftka, R. T. and Cinquini, C., "Optimization of Composite Plates for Buckling by Simulated Annealing", *Proc.* AIAA/ASME/ASCE/AHS/ASC Structures, Structural Dynamics, and Materials Conference, Dallas, Texas, April , 1992, pp. 2552-2562.

26. Chattopadhyay, A. and Seeley, C. E., "A Simulated Annealing Technique for Multiobjective Optimization of Intelligent Structures", *Journal of Smart Material and Structures*, Vol. 3, Feb. 1994, pp. 98-106.

27. Onoda, J. and Hanawa, Y., "Optimal Locations of Actuators for Statistical Static Shape Control of Large Space Structures: A Comparison of Approaches", *Proc. 33rd AIAA/ASME/ASCE/AHS/ASC Structures, Structural Dynamics and Materials Conference*, Dallas, Texas, April 13-15, 1992, pp. 2788-2795.

28. Agarwal, B. D and Broutman, L. J., Analysis and Performance of Fiber Composites, John Wiley and Sons, Inc., 1990, p. 437.

29. Chattopadhyay, A., McCarthy, T. R. and Seeley, C. E., "A Decomposition Based Optimization Procedure for High Speed Prop-Rotors using Composite Tailoring and Simulated Annealing," *Proc.* 50th Annual AHS Forum, Washington, DC, May 1994.

30. Acree, C. W. and Tischler, M. B., "Identification of XV-15 Aeroelastic Modes Using Frequency Sweeps," *Journal of Aircraft*, Vol. 26, No. 7, pp. 667-674, July 1989.

31. Johnson, W, "A Comprehensive Analytical Model of Rotorcraft Aerodynamics and Dynamics, Part II: User's Manual," NASA TM 81183, June 1980.

# Appendix - Nomenclature

## Roman

| | |
|---|---|
| $a_i$ | Simulated annealing design variable vector |
| $AI$ | Autorotational inertia, lb-ft$^2$ |
| $C$ | Wing chord, ft |
| $C_P$ | Coefficient of power |
| $C_T$ | Coefficient of thrust |
| $c$ | Blade chord, ft |
| $c_0$-$c_3$ | Blade chord distribution parameters |
| $c_d$ | Coefficient of drag |
| $c_l$ | Coefficient of lift |
| $c_{l\alpha}$ | Lift curve slope |
| $d_i$ | Design variables vector of pre-selected values |
| $EI_{xx}$ | Lagging stiffness, lb-ft$^2$ |
| $EI_{zz}$ | Flapping stiffness, lb-ft$^2$ |
| $F$ | Axial force, lb |
| $F_k$ | Vector of original objective functions |
| $F_k^*$ | Vector of reduced objective functions |
| $F_{KS}$ | K-S objective function |
| $f_1$ | First natural frequency in hover, per rev |
| $f_k$ | K-S function constraint vector |
| $FM$ | Hover figure of merit |
| $g_j$ | Original constraint vector |
| $GJ$ | Torsional rigidity, lb-ft$^2$ |
| $H$ | Interpolation matrix |
| $I_\theta$ | Polar moment of inertia, slug-ft$^2$ |
| $J$ | Propeller advance ratio ($\pi V_\infty/\Omega R$) |
| $k_{ij}$ | Stiffness matrix, p.s.i. |
| $k_r$ | Nondimensional blade radius of gyration |
| $L$ | Wing lift, lb |
| $M$ | Mach number |
| $M_{dd}$ | Drag divergence Mach number |
| $M_{tip}$ | Tip Mach number |

| | |
|---|---|
| $M_y$ | Flapping moment, lb-in |
| $M_z$ | Lagging moment, lb-in |
| $m$ | Blade sectional mass, slug/ft |
| NC | Number of constraints |
| NDV | Number of design variables |
| NF | Number of objective functions |
| NSEG | Number of blade segments |
| $P$ | Rotor power, hp |
| $p$ | Random number, $0 < p < 1$ |
| $P_{acc}$ | Acceptance probability |
| $p_n$ | Two-point exponential expansion exponent |
| $Q$ | Rotor Torque |
| $\overline{Q}_{ij}$ | Off-axis stiffness matrix for each lamina, p.s.i. |
| $Q_y$ | Transverse horizontal shear force, lb |
| $Q_z$ | Transverse vertical shear force, lb |
| $R$ | Blade radius, ft |
| $r$ | Radial location, ft |
| $r_c$ | Simulated annealing cooling rate |
| $T$ | Rotor thrust, lb |
| $T_k$ | Simulated annealing "temperature" |
| $t$ | Wall thickness, in |
| $t_{io}$-$t_{i3}$ | Wall thickness distribution parameters, ft |
| $t/c$ | Thickness to chord ratio |
| $u,\ v,\ w$ | Elastic displacements |
| $u_T$ | Swirl velocity, ft/s |
| $V_\infty$ | Forward velocity, ft/s$^2$ |
| $W$ | Resultant free stream velocity, ft/s$^2$ |
| $W_{blade}$ | Rotor blade weight, lb |
| $W_{total}$ | Combined wing/rotor weight, lb |
| $W_{wing}$ | Wing weight, lb |
| $\dot{w}$ | Wing flapping velocity, ft/s |
| $x,\ y,\ z$ | Reference axes |
| $X_a$ | Wing elastic axis offset, ft |
| $x_a/c$ | Lifting line offset |
| $\overline{y}$ | Nondimensional radial location, y/R |

## Greek

| | |
|---|---|
| $\alpha_b$ | Blade angle of attack, deg. |
| $\alpha_l$ | Local inflow angle, deg. |
| $\alpha_w$ | Wing angle of attack, rad. |
| $\alpha_{zl}$ | Zero lift angle, deg. |
| $\delta$ | K-S function draw down factor |
| $\varepsilon$ | Blade strain |
| $\Phi$ | Design variable vector |
| $\phi$ | Elastic twist |
| $\gamma_{\chi\eta}, \gamma_{\chi\zeta}$ | Shear strains |
| $\eta, \zeta$ | Local blade element axes |
| $\eta_c, \eta_t$ | Rotor propulsive efficiency |
| $\kappa$ | Box beam scaling factor |
| $\Lambda$ | Blade sweep, degrees |
| $\lambda$ | Taper ratio |
| $\Lambda_k$ | Real part of the kth stability root |
| $\lambda_w$ | Out of plane warping function |
| $\mu$ | Helicopter advance ratio $(V_\infty/\Omega R)$ |
| $\theta$ | Blade twist, degrees |
| $\theta_1-\theta_3$ | Blade twist distribution parameters |
| $\theta_{75}$ | Blade collective pitch angle, deg |
| $\rho_\infty$ | Air density, slug/ft$^3$ |
| $\sigma_1, \sigma_2$ | Material axis normal stresses, p.s.i. |
| $\sigma_{al}$ | Allowable stress, p.s.i. |
| $\tau_{12}$ | Shear stress, p.s.i. |
| $\tau_{oct}$ | Octahedral wing stress, p.s.i. |
| $\upsilon_i$ | Inflow velocity, ft/s |
| $\Omega$ | Rotor angular velocity, r.p.m. |

$\zeta$            Nondimensional wing span, y/b

## Subscripts

| | |
|---|---|
| c | High speed cruise |
| h | Hover |
| max | Maximum allowable |
| ref | Reference, or baseline, value |
| t | Take-off |